The Astronomical Journal, 129:2074–2101, 2005 May

A COMPLETE MULTIWAVELENGTH CHARACTERIZATION OF FAINT *CHANDRA* X-RAY SOURCES SEEN IN THE *SPITZER* WIDE-AREA INFRARED EXTRAGALACTIC (SWIRE) SURVEY

Alberto Franceschini and James Manners
Dipartimento di Astronomia, Universita di Padova, Vicolo Osservatorio 5, I-35122 Padua, Italy

Maria del Carmen Polletta
Center for Astrophysics and Space Sciences, University of California at San Diego, La Jolla, CA 92093-0424

Carol Lonsdale
Infrared Processing and Analysis Center, California Institute of Technology, MS 100-22, Pasadena, CA 91125

Eduardo Gonzalez-Solares
Institute of Astronomy, University of Cambridge, Madingley Road, Cambridge CB3 0HA, UK

Jason Surace, Dave Shupe, Fan Fang, C. Kevin Xu, and Duncan Farrah
Infrared Processing and Analysis Center, California Institute of Technology, MS 100-22, Pasadena, CA 91125

Stefano Berta and Giulia Rodighiero
Dipartimento di Astronomia, Universita di Padova, Vicolo Osservatorio 5, I-35122 Padua, Italy

Ismael Perez-Fournon and Evanthia Hatziminaoglou
Instituto de Astrofisica de Canarias, 38200 La Laguna, Tenerife, Spain

Harding E. Smith and Brian Siana
Center for Astrophysics and Space Sciences, University of California at San Diego, La Jolla, CA 92093-0424

Michael Rowan-Robinson, Kirpal Nandra, Tom Babbedge, and Mattia Vaccari
Astrophysics Group, Blackett Laboratory, Imperial College, Prince Consort Road, London SW7 2BW, UK

Seb Oliver
Astronomy Centre, University of Sussex, Brighton BN1 9QJ, UK

Belinda Wilkes
Harvard-Smithsonian Center for Astrophysics, Cambridge, MA 02138

Frazer Owen
National Radio Astronomy Observatory, P.O. Box O, Socorro, NM 87801

Deborah Padgett, Dave Frayer, Tom Jarrett, and Frank Masci
Infrared Processing and Analysis Center, California Institute of Technology, MS 100-22, Pasadena, CA 91125

Gordon Stacey
Department of Astronomy, Cornell University, 220 Space Science Building, Ithaca, NY 14853

Omar Almaini
School of Physics and Astronomy, University of Nottingham, University Park, Nottingham NG7 2RD, UK

Richard McMahon
Institute of Astronomy, University of Cambridge, Madingley Road, Cambridge CB3 0HA, UK

Olivia Johnson and Andrew Lawrence
Institute for Astronomy, University of Edinburgh, Royal Observatory, Blackford Hill, Edinburgh EH9 3HJ, UK

and

Chris Willott
Herzberg Institute of Astrophysics, National Research Council, 5071 West Saanich Road, Victoria, BC V9E 2E7, Canada
Received 2004 September 3; accepted 2004 December 13

ABSTRACT

We exploit deep combined observations with *Spitzer* and *Chandra* of the *Spitzer* Wide-Area Infrared Extragalactic Survey (SWIRE) in the ELAIS N1 region to investigate the nature of the faint X-ray and IR sources in common, to identify active galactic nucleus (AGN)/starburst diagnostics, and to study the sources of the X-ray and IR cosmic backgrounds (XRB and CIRB). In the $17' \times 17'$ area of the *Chandra* ACIS-I image there are approximately 3400 SWIRE near-IR sources with 4 σ detections in at least two Infrared Array Camera (IRAC) bands and 988 sources detected at 24 μm with the Multiband Imaging Photometer (MIPS) brighter than $S_{24} \simeq 0.1$ mJy. Of these, 102 IRAC and 59 MIPS sources have *Chandra* counterparts, out of a total of 122 X-ray sources present in the area with $S_{0.5-8\,\mathrm{keV}} > 10^{-15}$ ergs cm^{-2} s^{-1}. We have constructed spectral energy distributions (SEDs) for each source using data from the four IRAC wavebands, *Chandra* fluxes in the hard (2–8 keV) and soft (0.5–2 keV) X-rays, and optical follow-up data in the wavebands U, g', r', i', Z, and H. We fit a number of spectral templates to the SEDs at optical and IR wavelengths to determine photometric redshifts and spectral categories and also make use of diagnostics based on

the X-ray luminosities, hardness ratios, X-ray to IR spectral slopes, and optical morphologies. Although we have spectroscopic redshifts for only a minority of the *Chandra* sources (10 type 1 QSOs or Seyfert sources and three galaxies), the available SEDs constrain the redshifts for most of the sample sources, which turn out to be typically at $0.5 < z < 2$. We find that 39% of the *Chandra* sources are dominated by type 1 AGN emission (QSOs or Seyfert 1), 23% display optical/IR spectra typical of type 2 AGNs, while the remaining 38% show starburst-like or even normal galaxy spectra (including five passively evolving early-type galaxies). Since we prove that all these galaxies are dominated by AGN emission in X-rays (considering their large 0.5–8 keV rest-frame X-ray luminosities and their high X-ray to IR flux ratios), this brings the fraction of type 1 AGNs to 80% of the type 2 AGNs; even assuming that all the *Chandra* sources undetected by *Spitzer* are type 2 AGNs, the type 1 fraction would exceed 1/3 of the total population. Our analysis of the mid-IR MIPS 24 μm–selected sources, making up $\sim$50% of the CIRB, shows that the fraction of those dominated by an AGN (either type 1 or type 2) is relatively constant with the IR flux and around 10%–15%. Our combined IR and hard X-ray observations allow us to verify that the dust covering fraction in type 1 AGNs is widely distributed between $\sim$10% and 100%. A significant fraction, from 15% to 30% or more, of the sources of the XRB are hosted in galaxies whose optical/IR spectra are dominated by starburst (or normal galaxy) emission and for which only the hard X-ray spectra reveal the presence of a moderately luminous hidden AGN.

Key words: galaxies: evolution — quasars: general — X-rays: galaxies

1. INTRODUCTION

The *Spitzer Space Telescope* is providing a new sensitive tool for cosmological investigations over a wide spectral region from 3 to 160 μm. The *Spitzer* Wide-Area Infrared Extragalactic Legacy Survey (SWIRE) in particular, with its large areal and IR spectral coverage, will not only allow us to quantify the role of the environment in structure formation and evolution but is also providing rich enough statistical samples for investigating relatively rare source populations (Lonsdale et al. 2003, 2004).

The sources of the cosmic X-ray background (XRB), efficiently detected by *Chandra* and *XMM-Newton*, belong to this last category of relatively uncommon objects. Recently, the importance of combined hard X-ray and mid- and far-IR data for testing the active galactic nucleus (AGN) unification model and for verifying the standard obscured accretion paradigm for the origin of the XRB has been emphasized (Risaliti et al. 2000; Franceschini et al. 2002; Fadda et al. 2002; Alonso-Herrero et al. 2004; Rigby et al. 2004; Manners et al. 2004; Alexander et al. 2003). Indeed, a relationship has been suggested to hold between the XRB and the more recently discovered cosmological background in the far-IR, the CIRB (Puget et al. 1996; Hauser et al. 1998). The X-ray emission that is photoelectrically absorbed in the type 2 AGNs dominating the XRB is expected to be downgraded in energy by the dusty circumnuclear medium and to emerge thermally reprocessed in the IR between a few and a few hundred microns (e.g., Granato et al. 1997). An important test of this picture is then provided by detection in the IR of the downgraded energy absorbed in X-rays.

A related aspect is to investigate how the X-ray and UV/optical absorbed flux from AGNs contributes to explaining the energetics of the IR sources and of the whole IR background itself. Considering that the CIRB contains more than half of the total radiant energy produced by cosmic sources (Hauser & Dwek 2001; Franceschini et al. 2001), it is of crucial importance to assess the physical origin of this component. The issue is still relatively unsettled, with the expected AGN fraction ranging from 50% of the CIRB being due to AGNs (under some extreme assumptions about the IR emissivity of type 2 objects and the percentage of Compton-thick sources; see Almaini et al. 1999; Fabian & Iwasawa 1999) to a few percent (Elbaz et al. 2002).

The first attempts to answer these questions were based on the pioneering mid-IR sky surveys with the *Infrared Space Observatory* (*ISO*). Fadda et al. (2002) detected 24 sources in common between *ISO* at 15 μm and *XMM-Newton* in an area of the Lockman Hole. On that basis, Fadda et al. and Franceschini et al. (2002) concluded that the expectations of the obscured accretion model are basically met. These studies also suggested that only a minor fraction of the CIRB seems to be due to gravitational accretion. These conclusions were, however, limited by small-number statistics and by poor spectral coverage of the source spectral energy distributions (SEDs) (essentially limited to the 15 μm data point).

In addition, deep long-wavelength surveys with SCUBA and MAMBO have been cross-correlated with ultradeep *Chandra* images, with the result that although many high-z submillimeter SCUBA sources show detectable hard X-ray emission, the large majority of the bolometric flux does not appear to be due to an AGN (Alexander et al. 2005). In any case, not much can be concluded from these data about the origin of the CIRB, because it is still uncertain how much the submillimeter sources contribute to the CIRB at its peak at around 100 μm. This is also made uncertain by a quite complicated source selection function (including submillimeter and radio/optical identification) and, again, poor statistics.

We report in this paper a refined analysis of the relationship between X-ray and IR emission for faint cosmic sources over a wide redshift interval based on combined *Spitzer* and *Chandra* observations of an area in ELAIS N1. This region has been previously observed with *ISO* as part of the ELAIS survey (Oliver et al. 2000). *ISO* detected six extragalactic sources at 15 μm within the $17' \times 17'$ area of the ELAIS N1 *Chandra* ACIS-I image, three of which have detectable counterparts in X-rays, according to Manners et al. (2004).

For comparison, the present SWIRE survey in the same small area detects $\sim$900 sources at 24 μm above $S_{24} = 100$ μJy and 3500 Infrared Array Camera (IRAC) near-IR galaxies. We find that 102 (84%) of the 122 *Chandra* sources in the ACIS-I area now have mid- and far-IR counterparts from *Spitzer*.

The *Spitzer Space Telescope*, *Chandra*, and ancillary optical observations of the ELAIS N1 region are detailed in § 2. Particular attention is paid here to the estimation of photometric redshifts for our sample sources, given that only a fraction of them have optical spectroscopic data. Although our approach is similar to others recently published for X-ray–selected source populations (Franceschini et al. 2002; Zheng et al. 2004), our advantage here is to benefit from an accurate coverage of the near- and mid-IR spectrum with the four IRAC channels centered at 3.6, 4.5, 5.8, and 8 μm and the Multiband Imaging Photometer for *Spitzer* (MIPS) 24 μm channel.

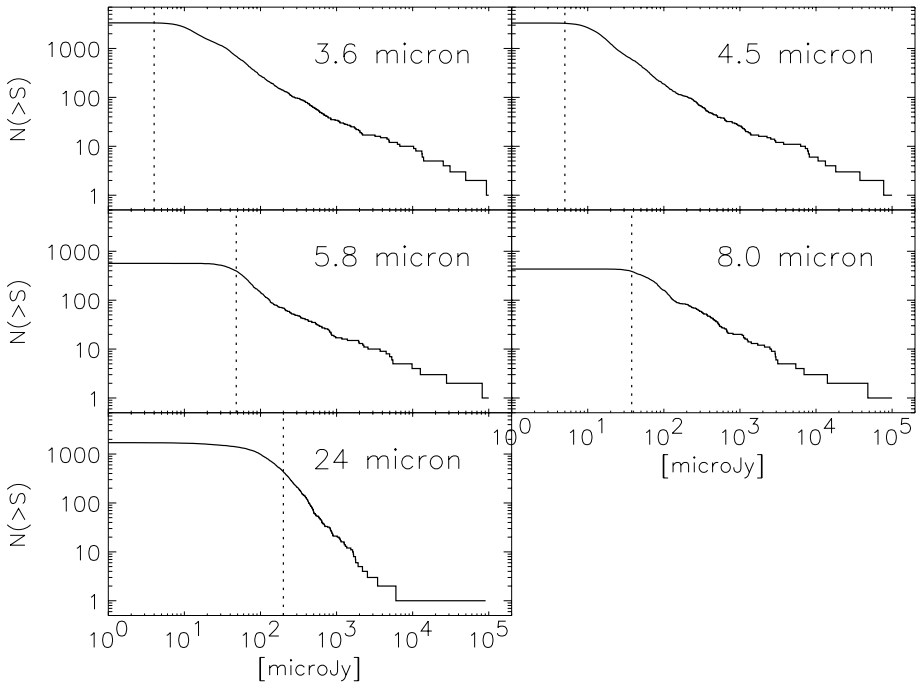

FIG. 1.—Cumulative number counts of galaxies detected with signal-to-noise ratio >4 by *Spitzer* within the 286 square arcmin of the *Chandra* ACIS-I image. The vertical dotted lines mark the limiting fluxes for 90% completeness.

The main results of our analysis are reported in § 3, in which we detail the X-ray and IR cross-correlation and source identification procedures, the analysis of the SEDs and classification of the sources, and the X-ray to IR flux correlations and color and hardness ratio plots. We discuss, in particular, new diagnostic diagrams for AGN- and galaxy-dominated emission in the optical/IR based on structural differences in the spectra. Photometric redshifts are used to infer important statistical information on redshift and luminosity distributions. The X-ray and IR identification statistics and some inferences about the AGN dust covering, as well as a comparison of *Chandra*-detected and *Chandra*-undetected SWIRE populations, are also addressed in § 3. The paper's conclusions are summarized in § 4.

2. OBSERVATIONS

2.1. *Spitzer Space Telescope Observations*

The SWIRE ELAIS N1 field was imaged by the IRAC multiband camera on *Spitzer* in 2004 January and with MIPS in early 2004 February, following the strategy described in Lonsdale et al. (2004). The original observing plan was corrected after the *Spitzer* performance verification (PV) phase by increasing the depth of the MIPS coverage to account for a reduced efficiency of the 70 μm channel. The observations were centered at the position ($16^{h}00^{m}$, $+59^{\circ}01'$).

Data processing began with the *Spitzer* Basic Calibrated Data (BCD), corrected for bias offsets and pixel-to-pixel gain variations (flat-fielding) and flux-calibrated in surface brightness. Additional IRAC processing corrected for latent images and electronic offsets. For MIPS, scan-mirror–dependent flats were derived from the data and applied to the BCD images. Individual images, which have measurable spatial distortions, were reprojected onto a single common projection system on the sky and co-added after correction for cosmic rays and other transient artifacts.

Fluxes were extracted in 5.″8 apertures for IRAC ($\sim$2–3 times the FWHM beam) and 12″ apertures for MIPS 24 μm using SExtractor. Sources are typically unresolved by the large *Spitzer* beams (>2″ at the shortest wavelength). The absolute flux calibrations are believed to be correct within roughly 10% for the IRAC and for the MIPS 24 μm channel data and were confirmed for IRAC by comparison to the Two Micron All Sky Survey (2MASS). The resulting catalogs were examined by eye, and remaining spurious sources (radiation, scattered light, etc.) were removed by hand. More details on the data processing are given in Surace et al. (2005) and Shupe et al. (2005).

The achieved sensitivities with the SWIRE survey in ELAIS N1 turned out to be deeper than preflight expectations in the two short-wavelength IRAC channels and in the MIPS 24 μm one, while performing less well in the other bands. The integral number counts of *Spitzer* sources in the *Chandra* ACIS-I 286 square arcmin field are reported in Figure 1. Dotted vertical lines mark the flux limits corresponding to 90% completeness limits, as determined from the deviation of the observed number counts from a power law and from simulations (Shupe et al. 2005).

2.2. *The X-Ray Data*

The X-ray observations were taken as part of the ELAIS Deep X-ray Survey (EDXS) and are described in detail in Manners et al. (2003). For this analysis we use the *Chandra* Advanced CCD Imaging Spectrometer (ACIS) observation of 75 ks centered on ($16^{h}10^{m}20^{s}.11$, $+54^{\circ}33'22''.3$) (J2000.0) in the ELAIS N1 region. The aim point was focused on the ACIS-I chips, which consist of four CCDs arranged in a 2×2 array covering an area of $16'.9 \times 16'.9$ (286 square arcmin). Bad pixels and columns were removed, and data were filtered to eliminate high background times (due to strong solar flares), leaving 71.5 ks of good data after filtering. Source detection and characterization in three bands (0.5–8 keV [full band], 0.5–2 keV [soft band], and 2–8 keV [hard band]) were achieved using the *wavdetect* software package (Freeman et al. 2002). For each band, exposure maps were constructed to account for variations in effective exposure across an image and used to remove bias from the source detection

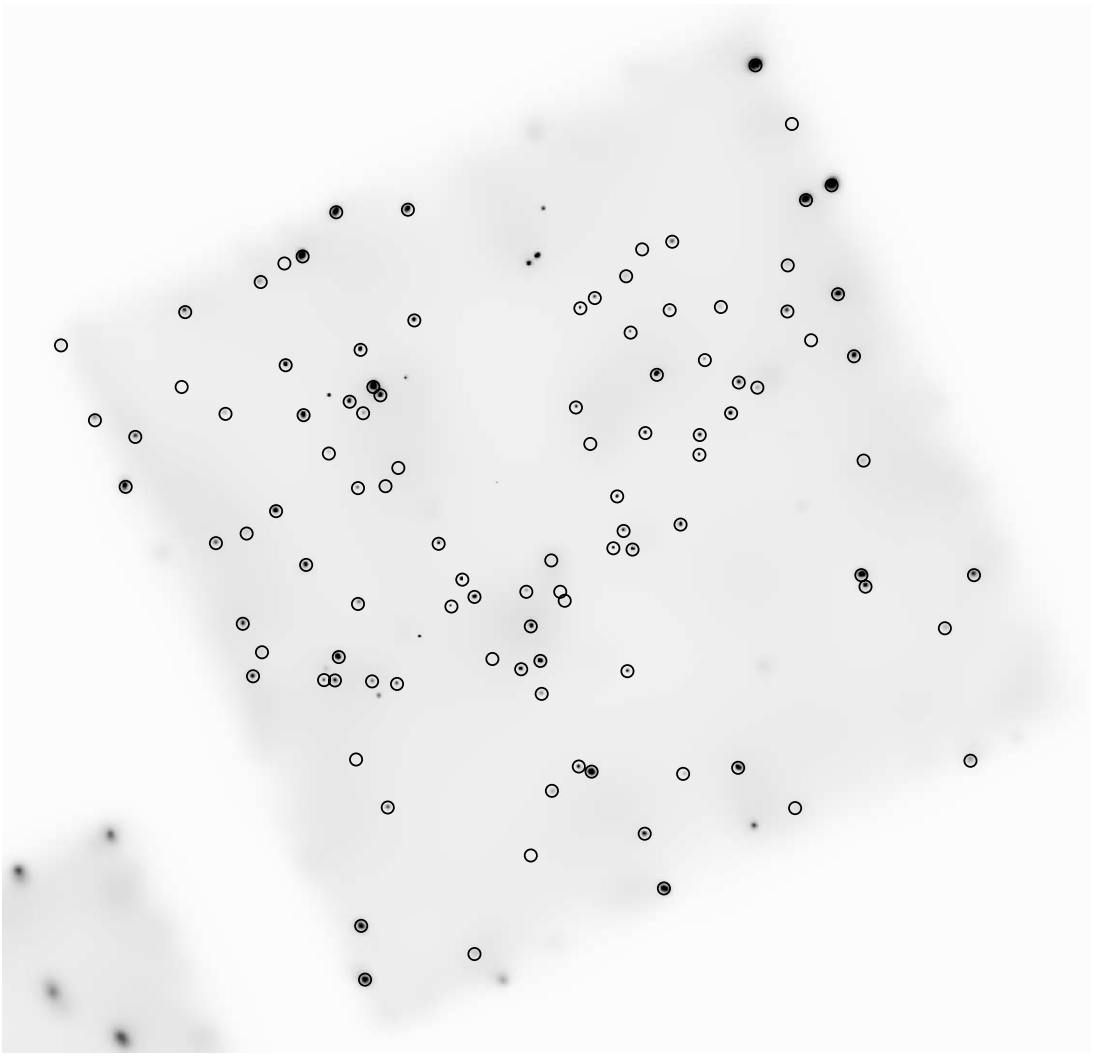

FIG. 2.—Adaptively smoothed *Chandra* image overlaid with positions for 102 sources detected by *Spitzer* with IRAC.

and to calculate source fluxes. Counts-to-photon calibration assumed a standard power-law model spectrum with photon index $\Gamma = 1.7$.

Sources were detected to flux levels of 2.3×10^{-15} ergs s^{-1} cm^{-2} in the 0.5–8 keV band, 9.4×10^{-16} ergs s^{-1} cm^{-2} in the 0.5–2 keV band, and 5.2×10^{-15} ergs s^{-1} cm^{-2} in the 2–8 keV band. Sources are detectable to these flux limits over 90% of the nominal survey area. For this analysis we used sources detected in the full band of ACIS-I only, of which there are 122 in the N1 region. Of the 102 sources in common between *Chandra* and SWIRE, 83 have significant detections in the separate soft X-ray band (0.5–2 keV) and 64 are detected in the hard (2–8 keV) band.

The smoothed 0.5–8 keV *Chandra* ACIS-I image is reported in Figure 2 with the associated SWIRE sources overlaid. The image has been adaptively smoothed using the flux-conserving algorithm *csmooth* from the *Chandra* Interactive Analysis of Observations (CIAO) package. We defer to Manners et al. (2003, 2004) for more details on the X-ray data reduction and analysis.

2.3. *The Optical Data*

Follow-up observations of the EDXS sources have been taken in the bands *U*, *g*, *r*, *i*, and *H* and are detailed in Gonzalez-Solares et al. (2004). The Wide-Field Camera (WFC) on the Isaac Newton Telescope (INT) was used to observe a $30' \times 30'$ region centered on the *Chandra* N1 pointing. Data were observed in the *g*, *r*, and *i* bands in 2000 July and in the *U* band in 2001 June using the Sloan Digital Sky Survey (SDSS) photometric system. Total integration times were 100 minutes in the *g*, *r*, and *i* bands and 120 minutes in the *U* band, reaching Vega magnitude limits for a pointlike source in an aperture of 3″ of $U = 24.0$, $g = 25.5$, $r = 25.2$, $i = 24.1$, and $H = 20.5$. Because of potential source variability and the different observing time, the *U*-band data have significant uncertainty that has been taken into account in the subsequent analysis.

H-band observations were carried out in 2000 June using the Cambridge Infrared Survey Instrument (CIRSI) at the INT. The *H* filter is centered at 1.65 μm with a width (FWHM) of 0.3 μm and a transmission peak of 75%. A total integration of 60 minutes was taken over the $30' \times 30'$ used for the previous observations.

For several of our sources we also used fluxes in the *Z* band taken with the INT by Babbedge et al. (2005, the Wide-Field Survey).

All the images have been registered to a common world coordinate system and resampled to a common pixel scale. This step allowed us to carry out the detection in one reference image

and the flux measurements in the others. This alleviates the task of cross-correlating different catalogs and allows us to measure magnitudes using the same aperture in all the images, as appropriate for SED analysis and required for the calculation of photometric redshifts. Source detection was performed using SExtractor (Bertin & Arnouts 1996). The measured parameters include positions and positional errors, basic shape parameters as well as elongation and ellipticity, and different types of fluxes and magnitudes: isophotal, corrected isophotal, fixed aperture, and Kron-like automatic aperture, as well as errors. The automatic aperture magnitude is designed to give the most precise flux measure and is the one used as the magnitude in this work. For the above-mentioned reasons, we require the magnitudes to be measured in the same aperture in each band. The object detection and aperture estimation is performed in the *r*-band images, and then magnitudes are obtained on all the images using that aperture. Since there are some X-ray objects that fall in the gaps between *r*-band chips, a second catalog was created by taking as the reference the *g*-band image. The absolute photometry was tied to the Wide-Field Survey (optical) catalog already existent in that area and 2MASS (IR) using bright nonsaturated stars. It was found that 85% of the X-ray sources have an optical counterpart, a fraction comparable to the detection rate achieved with *Spitzer* IRAC.

2.4. *Redshift Measurements*

Spectroscopic redshifts are available for only 13 of the 99 extragalactic sources in common between *Chandra* and *Spitzer*. These include six type 1 QSOs and two low-redshift galaxies observed by Gonzalez-Solares et al. (2005, including details on this optical spectroscopic run). Additional optical spectroscopy has been obtained at Palomar with the COSMIC spectrograph on 2004 June 10 and 11, providing the redshift for five further sources (two type 1 and two type 2 AGNs and a galaxy).

For the remaining objects, and thanks to the good coverage of the near- and mid-IR spectrum with the four IRAC channels, we estimated photometric redshifts with a tool based on the Hyper-*z* code (Bolzonella et al. 2000), as discussed in detail by Polletta et al. (2005). Hyper-*z* allowed a large database of galaxy spectra to be synthesized, including the effects of dust extinction. The following parameter ranges have been explored with Hyper-*z*: A_V between 0 and 0.7, redshifts between 0 and 3.5, and absolute magnitudes in the g' band between -19 and -26. As expected, for the typical SEDs of our sample objects, the redshift estimates turned out to be rather insensitive to the amount of extinction.

Similar photometric redshift approaches have been successfully attempted for X-ray–selected source populations (Franceschini et al. 2002; Zheng et al. 2004), in which cases a comparison with spectroscopic measurements has revealed fair accuracy in the procedure (errors $\delta z \sim 0.1$). Independent photometric redshift estimates for SWIRE galaxy samples are reported in Rowan-Robinson et al. (2005; see also Rowan-Robinson 2003) and by Babbedge et al. (2004). Fair agreement between these codes is found by Babbedge et al., although in the current case the *z*-estimate is made more uncertain by the more complex nature of SEDs of AGN host galaxies.

Given the typical optical/IR SEDs of our sources, we expect that the photometric redshifts are more accurate for galaxy-dominated spectra and type 2 AGNs, which together make up the majority in our sample. Obviously, for the typically flat and featureless SEDs of type 1 QSOs, they are expected to be much less reliable. This expectation is confirmed by a comparison of photometric and spectroscopic redshifts for our 13 spectroscopically identified sources.

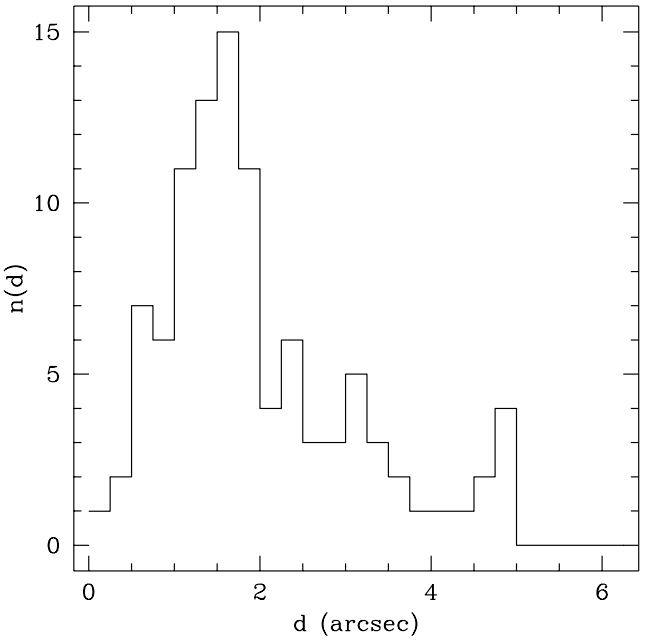

FIG. 3.—Distribution of positional distances between the centroids of the 3.6 μm sources and the *Chandra* sources. The distribution includes a slight systematic offset in declination, also apparent in Fig. 2, which, however, does not influence the source identification.

3. RESULTS

3.1. *Cross-Correlation Analysis and Source Identification*

A simple near-neighbor search has been performed to cross-correlate the *Spitzer* and *Chandra* source catalogs within the *Chandra* ACIS-I chip image, using a $d = 5''$ search radius (roughly the quadratic sum of the astrometric errors). The distribution of separations between the *Chandra* and *Spitzer* centroids is reported in Figure 3.

The *Spitzer* source catalog used for the cross-correlation was a subset of the full band-merged catalog for the IRAC and MIPS 24 μm bands. It contained only those sources with a signal-to-noise ratio greater than 4 in at least two of the *Spitzer* bands. This catalog contained 3420 objects within the region of the *Chandra* ACIS-I image, compared with the 122 *Chandra* full-band detections.

All together, we find reliably associated counterparts for 102 of the 122 *Chandra* sources (84% in total). The vast majority of these are detected with the IRAC channels 1 and 2 (3.6 and 4.5 μm): 100 of the 122 *Chandra* sources in each case. Such an identification fraction decreases when considering the longer wavelength IRAC channels or MIPS. As many as 59 *Chandra* objects are reliably associated with MIPS 24 μm sources (all of them having IRAC counterparts), and just 1 had a MIPS 70 μm counterpart. More details on the source identification statistics are reported in Table 1, where the first column indicates the *Spitzer* band, the second indicates the number of *Spitzer* sources detected above the 4 σ limiting flux $S_{\rm lim}$ (reported in the third column), the fourth column gives the number of *Chandra* sources identified in the various channels, and the fifth shows their percentage over the total number of *Spitzer* sources.

To estimate the reality of the associations, we have calculated the probability of random matches between the X-ray sources and the possible *Spitzer* counterparts. As discussed in Fadda

TABLE 1
IDENTIFICATION STATISTICS OF *Spitzer* AND *Chandra* SOURCES

SWIRE Channel	SWIRE Sources	$S_{\rm lim}$ (μJy)	*Chandra* Detections	Percentage
IRAC 1.....	3342	6	100	3.0
IRAC 2.....	3306	6	100	3.0
IRAC 3.....	559	25	56	10.0
IRAC 4.....	432	32	51	11.8
MIPS 24.....	988	100	59	6.0

et al. (2002), we assume the IR population to follow a Poisson spatial distribution, such that the probability P of a random association is

$$P = 1 - e^{-N\pi d^2}, \quad (1)$$

where d is the offset distance between the X-ray and *Spitzer* source and N is the areal number density of possible *Spitzer* counterparts derived from Figure 1. The probability P turned out to be sufficiently small to guarantee that almost all our associations are real. Approximately 90% have $P < 0.03$. Summing the probabilities, we expect two false associations in the 102 matched sources.

Only three *Chandra* sources have multiple associations within 5″ in the IRAC images. Of these, two (N1_8 and N1_81) have been unambiguously identified, as they lie near to the center of the *Chandra* image, where the *Chandra* point-spread function (PSF) is small. Since the positional accuracy is dominated by the size of the *Chandra* PSF, we can reliably reject any associations with offsets greater than the 3 σ size of the *Chandra* PSF for these sources, leaving only one association in each case. The third source (N1_104) is near the edge of the *Chandra* image and therefore has a large *Chandra* PSF that contains two *Spitzer* sources (as well as two optical sources) within the 3 σ PSF extent. We assume the association to be the *Spitzer* source closest to the center of the *Chandra* PSF and closest to the central optical source. This appears justified by the observed Seyfert-type spectrum found for this object (see Fig. 5*h* below).

Of the 102 *Spitzer*-identified *Chandra* sources, three turned out to correspond to Galactic stars on the basis of their position on color-magnitude plots and optical morphology and are excluded from our subsequent analysis.

We report in Figure 4 histograms of the ratio of the X-ray flux (in the total 0.5–8 keV band) to the 3.6 and 24 μm fluxes for sources detected by SWIRE in the *Chandra* area brighter than 5 and 100 μJy, respectively. The figure compares the flux ratio distributions for sources with *Chandra* counterparts (*solid-line histograms*) and those without *Chandra* associations (*shaded histograms*). The latter are the distribution of the upper limits on the flux ratios computed using the *Chandra* 3 σ X-ray sensitivity limits, as in § 2.2.

The arrows in the top panel of Figure 4 indicate the observed values of the flux ratios for representative active galaxies: type 1 (A: NGC 4151) and type 2 AGNs (B: NGC 6240; C: IRAS 19254s), an ultraluminous IR quasar with high X-ray absorption (E: Mrk 231), and a low-luminosity starburst (D: M82). For these sources, the 24 μm flux ($\nu_{24}S_{24}$) is estimated from the 25 μm *IRAS* data, while the X-ray data are taken from George et al. (1998), Cappi et al. (1999), Franceschini et al. (2003), and Braito et al. (2004). X-ray to IR flux ratios in our *Chandra* sample are then typical of X-ray–luminous AGNs and definitely larger than those of starburst galaxies or even heavily absorbed type 2 QSOs.

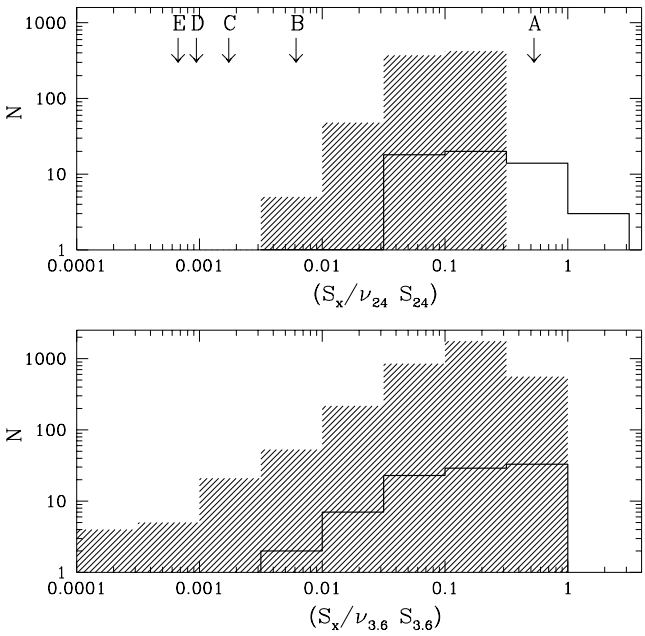

FIG. 4.—*Top:* Histograms of the ratio of the 0.5–8 keV band X-ray flux (S_X) to the 24 μm flux for sources detected by SWIRE in the area covered by *Chandra*. The solid-line histogram refers to sources with *Chandra* counterparts, while the shaded histogram is the distribution of upper limits for those without *Chandra* associations. *Bottom:* Same as top panel for the IRAC 3.6 μm sources. Our adopted flux limits for the SWIRE samples are 5 and 100 μJy for 3.6 and 24 μm, respectively. In the top panel the arrows indicate the values of representative active galaxies: A, NGC 4151; B, NGC 6240; C, IRAS 19254s; D, M82; and E, Mrk 231.

3.2. *Analysis of the Spectral Energy Distributions*

The positions, *Spitzer* IRAC and MIPS data, X-ray fluxes, spectral classifications, X-ray hardness ratios, and luminosities for our SWIRE-*Chandra* sample are reported in Table 2. The excellent UV/optical/IR spectral coverage available for our sources has prompted us to perform a very extensive analysis based on the Hyper-*z* code (Bolzonella et al. 2000) and a wide variety of additional spectral templates, aimed at a physical characterization of the sources.

Basically, starburst-dominated and quasar-dominated sources can be discriminated on the basis of the presence or absence of the classical UV excess and flat optical SED in type 1 QSOs or from the mid-IR excess characterizing the spectra of both type 1 and type 2 AGNs. The latter is due to emission of very hot dust with temperatures close to the grain sublimation temperature and is essentially missing in purely starburst regions. We defer to Berta et al. (2003) and Prouton et al. (2004) for further discussion about this point. The diagnostic power offered by full UV/optical/IR spectral coverage for disentangling AGNs and starbursts can be appreciated by considering that the typical peak around 1 μm of the integrated emission of stellar populations in normal galaxies roughly (and coincidentally) corresponds to a minimum of the spectrum of quasar nuclei between the UV "big bump" and the near-IR hot dust component. We further discuss this point in subsequent sections.

While an exhaustive description of the spectral database used for our analysis can be found in Polletta et al. (2005), we summarize here its main features. It consists of 22 spectral templates that are derived from the observed SEDs of various galaxy

TABLE 2

RELEVANT DATA ON THE *Spitzer* AND *Chandra* SOURCE SAMPLE

ID (1)	R.A. (deg) (2)	Decl. (deg) (3)	$S_{3.6}$ (mJy) (4)	$S_{4.5}$ (mJy) (5)	$S_{5.6}$ (mJy) (6)	S_{8} (mJy) (7)	S_{24} (mJy) (8)	d (arcsec) (9)	S_X (10^{-7} W cm^{-2}) (10)	δS_X (10^{-7} W cm^{-2}) (11)	Type (12)	HR (13)	$L_{0.5-8}$ (10^{-7} W) (14)
1	242.84070	54.56754	4.90 ± 0.799	15.3 ± 1.15	...	...	...	2.94	1.24E−14	1.53E−15	1	−0.31 ± 0.10	1.45E+44
2	242.80450	54.63007	7.94 ± 0.731	16.9 ± 1.16	...	...	120. ± 23.1	0.69	4.24E−15	8.81E−16	1	−0.44 ± 0.16	4.95E+43
3	242.76810	54.51849	17.4 ± 0.949	14.1 ± 1.14	...	...	...	0.68	4.33E−15	8.39E−16	3	0.03 ± 0.16	2.09E+43
4	242.74789	54.55882	66.8 ± 1.27	68.6 ± 1.5	134. ± 6.42	235. ± 6.43	637. ± 24.9	1.15	1.61E−14	1.50E−15	2	−0.34 ± 0.08	7.77E+43
5	242.74207	54.61105	10.7 ± 0.853	9.74 ± 1.06	...	...	45.0 ± 20.3	1.94	8.10E−15	1.07E−15	3	−0.40 ± 0.12	5.95E+43
6	242.73192	54.64997	80.3 ± 1.23	79.2 ± 1.55	110. ± 5.21	140. ± 6.01	351. ± 19.7	2.26	2.63E−14	1.94E−15	2	−0.25 ± 0.07	6.93E+43
8	242.73097	54.59314	52.7 ± 1.17	51.5 ± 1.41	72.6 ± 5.86	109. ± 6.2	578. ± 20.8	1.70	1.71E−14	1.56E−15	1	−0.53 ± 0.07	1.09E+44
9	242.72926	54.53955	16.5 ± 1.06	...	...	31.7 ± 5.68	49.2 ± 18.4	1.62	7.41E−15	1.03E−15	1	−0.40 ± 0.12	5.86E+43
10	242.71800	54.49846	32.6 ± 0.954	28.3 ± 1.1	40.9 ± 4.56	51.5 ± 4.43	167. ± 22.5	1.38	1.66E−15	5.29E−16	1	−0.27 ± 0.28	6.36E+42
12	242.71112	54.49831	8.82 ± 0.717	12.9 ± 0.922	...	...	...	1.59	4.08E−15	8.08E−16	3	0.39 ± 0.17	3.15E+43
13	242.71115	54.66571	38.0 ± 0.858	46.6 ± 1.12	52.0 ± 4.59	85.2 ± 4.55	223. ± 19.4	4.57	1.54E−14	1.50E−15	1	−0.24 ± 0.08	6.16E+43
14	242.70901	54.50658	41.6 ± 0.867	57.7 ± 1.2	58.9 ± 4.3	89.0 ± 4.87	...	1.42	1.95E−14	1.83E−15	1	−0.35 ± 0.08	1.60E+44
15	242.70256	54.59798	56.3 ± 1.2	64.5 ± 1.48	86.1 ± 6.08	116. ± 5.98	300. ± 23.3	0.81	1.06E−14	1.20E−15	1	−0.62 ± 0.09	1.14E+44
16	242.69814	54.47008	39.8 ± 0.977	25.6 ± 1.23	45.5 ± 5.64	...	...	3.23	1.47E−15	5.09E−16	3	0.60 ± 0.21	5.65E+42
18	242.69720	54.52565	24.9 ± 0.989	14.4 ± 1.14	...	...	...	3.07	2.43E−15	6.23E−16	3	−0.23 ± 0.22	9.30E+42
19	242.69609	54.61655	24.9 ± 0.803	14.5 ± 1.48	...	56.7 ± 5.76	...	1.26	6.55E−15	9.72E−16	1	−0.46 ± 0.13	2.78E+44
20	242.69415	54.59382	552. ± 3.31	355. ± 3.42	470. ± 12.3	2597 ± 13	1919 ± 30.9	1.21	2.31E−15	6.11E−16	3	−0.33 ± 0.24	2.35E+40
21	242.69202	54.39124	137. ± 2.02	105. ± 2.3	55.0 ± 5.75	93.4 ± 5.86	217. ± 21.4	1.53	1.86E−14	1.85E−15	3	−0.43 ± 0.08	7.12E+43
22	242.68829	54.49787	50.1 ± 1.22	42.5 ± 1.39	...	...	80.3 ± 22	0.37	2.40E−15	6.18E−16	3	0.92 ± 0.19	4.66E+42
23	242.68791	54.60337	479. ± 2.38	507. ± 2.76	640. ± 7.43	667. ± 6.48	1357 ± 23.2	1.49	3.59E−13	6.78E−15	1	−0.43 ± 0.01	4.02E+44
25	242.68373	54.60024	26.1 ± 0.838	25.5 ± 1.21	56.2 ± 4.73	...	114. ± 22.1	1.56	1.88E−14	1.57E−15	2	−0.30 ± 0.10	4.85E+44
26	242.67850	54.45293	106. ± 1.64	74.0 ± 1.71	60.6 ± 5.83	86.8 ± 5.83	400. ± 22.9	0.79	3.31E−15	7.38E−16	2	−0.54 ± 0.20	6.07E+42
27	242.67313	54.49701	18.3 ± 1.05	...	...	79.5 ± 5.8	346. ± 19.9	1.88	3.03E−15	7.47E−16	1	−0.33 ± 0.23	5.87E+43
28	242.67230	54.57432	17.1 ± 0.889	18.1 ± 1.3	...	...	188. ± 22.9	1.03	1.09E−15	4.15E−16	1	−1.03 ± 0.36	9.98E+42
30	242.66684	54.66679	39.2 ± 1.09	18.9 ± 1.28	...	...	129. ± 19.9	2.67	9.45E−15	1.17E−15	3	−0.28 ± 0.11	5.47E+42
31	242.66272	54.62717	73.7 ± 1.35	93.7 ± 1.67	252. ± 10.2	295. ± 6.38	1105 ± 22	2.0	7.81E−15	1.04E−15	2	−0.44 ± 0.12	6.56E+43
34	242.64740	54.54727	30.2 ± 0.999	23.7 ± 1.31	31.9 ± 5.66	...	9.85 ± 21	0.74	4.95E−15	8.16E−16	3	−0.48 ± 0.15	3.62E+43
38	242.63971	54.52485	85.2 ± 1.39	68.9 ± 1.65	35.6 ± 5.53	72.0 ± 5.79	317. ± 21	3.53	1.86E−15	5.08E−16	2	0.54 ± 0.26	6.92E+42
39	242.63295	54.53443	99	36.2 ± 1.35	40.0 ± 5.68	...	...	1.71	7.65E−15	1.13E−15	3	−0.09 ± 0.14	8.75E+43
40	242.62520	54.52821	19.5 ± 0.987	21.8 ± 1.37	74.8 ± 5.92	83.8 ± 5.84	289. ± 21.3	2.00	1.57E−14	1.41E−15	1	−0.32 ± 0.08	2.91E+43
41	242.61415	54.50594	32.9 ± 0.655	24.8 ± 1.25	40.6 ± 4.05	...	...	4.99	1.21E−15	4.47E−16	3	0.87 ± 0.30	4.65E+42
45	242.59665	54.50228	38.0 ± 1.1	29.0 ± 1.36	27.9 ± 5.63	73.6 ± 5.79	322. ± 19.6	1.65	5.90E−15	9.21E−16	2	0.46 ± 0.17	7.91E+42
46	242.59344	54.53010	27.5 ± 1.03	26.8 ± 1.3	...	...	...	1.06	1.48E−15	4.80E−16	2	0.39 ± 0.27	7.42E+42
48	242.59050	54.51771	87.5 ± 1.16	114. ± 1.82	140. ± 6.02	228. ± 6.36	498. ± 24.3	1.48	3.17E−14	1.98E−15	1	−0.43 ± 0.05	6.09E+44
50	242.58466	54.50531	111. ± 1.56	143. ± 1.94	162. ± 7.15	267. ± 6.32	861. ± 24	0.97	5.35E−14	2.59E−15	1	−0.52 ± 0.04	8.64E+43
51	242.58406	54.49353	14.1 ± 1.19	19.3 ± 1.23	...	...	...	1.99	1.86E−15	5.52E−16	3	0.02 ± 0.25	1.87E+43
53	242.57802	54.54125	4.92 ± 0.786	8.33 ± 1.09	...	...	14.4 ± 4.73	2.38	1.28E−15	4.47E−16	2	0.51 ± 0.28	1.85E+43
54	242.56976	54.52677	8.98 ± 0.571	10.6 ± 0.87	...	...	219. ± 19.7	1.02	1.32E−15	4.50E−16	2	0.34 ± 0.25	1.44E+43
55	242.56297	54.59608	60.8 ± 1.14	39.2 ± 1.2	...	...	...	0.57	3.34E−15	6.73E−16	3	−0.38 ± 0.18	1.92E+43

TABLE 2—*Continued*

ID (1)	R.A. (deg) (2)	Decl. (deg) (3)	$S_{3.6}$ (mJy) (4)	$S_{4.5}$ (mJy) (5)	$S_{5.6}$ (mJy) (6)	S_{8} (mJy) (7)	S_{24} (mJy) (8)	d (arcsec) (9)	S_X (10^{-7} W cm^{-2}) (10)	δS_X (10^{-7} W cm^{-2}) (11)	Type (12)	HR (13)	$L_{0.5-8}$ (10^{-7} W) (14)
56.....	242.56113	54.46746	12.1 ± 0.737	15.5 ± 0.948	...	...	...	1.03	3.24E−15	7.10E−16	3	0.03 ± 0.23	2.63E+43
57.....	242.56024	54.63151	37.0 ± 0.978	40.7 ± 1.22	57.4 ± 4.61	99.4 ± 5.27	81.5 ± 22.2	2.92	2.79E−15	6.65E−16	2	−0.12 ± 0.22	9.97E+43
58.....	242.55421	54.58305	15.4 ± 0.738	20.7 ± 1.2	46.6 ± 4.56	...	...	1.73	1.08E−15	4.16E−16	1	0.45 ± 0.33	3.20E+42
59.....	242.55330	54.46565	49.0 ± 0.966	59.9 ± 1.4	90. ± 5.33	118. ± 5.41	666. ± 27.3	0.35	2.83E−14	1.95E−15	1	−0.38 ± 0.06	4.41E+43
61.....	242.53992	54.54564	51.5 ± 0.964	26.5 ± 1.26	...	...	...	1.35	3.21E−15	6.78E−16	3	−0.44 ± 0.20	4.95E+42
62.....	242.53745	54.56409	80.2 ± 1.21	77.1 ± 1.27	76.2 ± 4.97	82.2 ± 4.75	341. ± 19.5	1.51	1.11E−14	1.80E−15	2	−0.67 ± 0.14	2.08E+44
64.....	242.53362	54.55189	33.4 ± 0.954	38.8 ± 1.11	55.5 ± 5.18	57.9 ± 4.35	471. ± 22.7	1.60	6.30E−15	9.03E−16	1	−0.89 ± 0.12	3.50E+44
65.....	242.53102	54.50165	6.42 ± 0.52	9.69 ± 0.783	...	...	...	0.91	4.78E−15	1.01E−15	1	0.09 ± 0.20	9.12E+43
66.....	242.52936	54.62281	4.18 ± 0.66	7.97 ± 1.12	...	...	130. ± 20.5	2.90	1.88E−15	5.42E−16	1	−0.87 ± 0.25	1.05E+44
67.....	242.52798	54.54510	55.6 ± 1.07	39.3 ± 1.35	49.6 ± 4.87	...	248. ± 24.4	1.64	2.22E−14	1.67E−15	1	−0.44 ± 0.06	7.25E+43
68.....	242.52010	54.58688	10.7 ± 0.841	11.8 ± 1.11	...	...	...	1.56	1.99E−15	5.59E−16	1	−0.59 ± 0.25	1.61E+43
69.....	242.51291	54.60775	243. ± 1.5	221. ± 1.84	168. ± 4.91	581. ± 7.21	1255 ± 21.1	2.12	5.95E−14	2.73E−15	3	−0.40 ± 0.04	1.25E+43
71.....	242.50871	54.42397	66.3 ± 1.14	56.9 ± 1.38	79.4 ± 5.1	81.2 ± 4.91	301. ± 20.5	1.84	1.58E−14	1.64E−15	1	−0.44 ± 0.09	2.42E+43
72.....	242.50519	54.63092	10.8 ± 0.833	7.96 ± 1.09	...	...	90.7 ± 22	1.13	2.03E−15	5.63E−16	3	0.70 ± 0.22	7.81E+42
73.....	242.50346	54.65526	49.7 ± 0.954	42.2 ± 1.2	76.1 ± 4.84	108. ± 4.83	438. ± 22.2	0.84	3.16E−15	7.37E−16	2	0.24 ± 0.21	1.07E+43
75.....	242.49825	54.55404	64.2 ± 1.28	103. ± 1.68	133. ± 6.9	210. ± 6.37	613. ± 21.4	1.83	1.61E−14	1.47E−15	1	−0.46 ± 0.08	1.99E+44
76.....	242.49693	54.46495	15.9 ± 0.751	...	...	...	257. ± 18.2	4.76	4.90E−15	1.31E−15	1	−0.27 ± 0.27	4.95E+43
77.....	242.48674	54.57907	7.06 ± 0.653	10.2 ± 0.811	...	...	...	2.68	3.37E−15	9.42E−16	1	−0.97 ± 0.29	1.68E+44
78.....	242.48642	54.58611	42.3 ± 1.04	53.3 ± 1	73.3 ± 5.22	108. ± 4.17	399. ± 24.1	1.38	3.79E−15	7.80E−16	2	−0.45 ± 0.18	6.91E+43
81.....	242.46735	54.59394	14.2 ± 0.986	25.5 ± 1.19	35.8 ± 5.61	50.8 ± 5.13	162. ± 23.7	1.82	5.75E−15	8.94E−16	1	−0.61 ± 0.13	1.48E+44
82.....	242.46300	54.46716	33.3 ± 1.06	25.8 ± 1.36	28.9 ± 5.49	...	...	1.79	9.49E−15	1.19E−15	2	−0.49 ± 0.11	5.84E+43
83.....	242.46237	54.60486	14.8 ± 0.865	14.0 ± 1.2	...	75.8 ± 5.97	288. ± 22.5	1.89	4.83E−15	8.92E−16	1	0.25 ± 0.17	1.06E+43
84.....	242.45204	54.71840	76.4 ± 1.33	103. ± 1.69	133. ± 6.46	202. ± 6.46	492. ± 22.4	4.94	4.29E−14	2.63E−15	1	−0.36 ± 0.05	6.71E+43
86.....	242.43242	54.63044	156. ± 1.81	111. ± 2.03	73.8 ± 5.9	80.0 ± 5.8	8.31 ± 22.7	2.45	3.75E−15	7.81E−16	3	−0.06 ± 0.17	7.89E+42
87.....	242.42087	54.67013	42.0 ± 0.873	56.7 ± 1.21	56.2 ± 5.24	88.3 ± 4.77	224. ± 20.3	1.98	1.98E−14	1.75E−15	1	−0.46 ± 0.08	7.95E+43
89.....	242.40501	54.67556	89.6 ± 1.5	50.9 ± 1.24	58.4 ± 5.15	83.4 ± 5.26	219. ± 20.8	0.61	4.31E−14	2.57E−15	2	−0.28 ± 0.05	1.49E+44
90.....	242.40094	54.63650	43.9 ± 1.11	50.0 ± 1.39	...	78.4 ± 6.22	325. ± 20.9	1.17	1.07E−14	1.27E−15	1	−0.46 ± 0.10	7.34E+43
92.....	242.39139	54.61434	185. ± 1.91	177. ± 2.08	215. ± 8.76	314. ± 6.39	889. ± 22.5	1.21	6.23E−15	9.73E−16	2	0.42 ± 0.12	2.23E+43
93.....	242.38696	54.53603	45.7 ± 0.989	32.8 ± 1.51	...	55.2 ± 5.74	71.3 ± 23.6	1.21	1.57E−14	1.50E−15	2	−0.33 ± 0.09	1.43E+44
94.....	242.38441	54.53204	11.1 ± 0.692	10.1 ± 0.906	...	...	197. ± 22.7	1.42	6.00E−15	9.81E−16	1	−0.27 ± 0.15	1.26E+44
95.....	242.31757	54.53606	53.1 ± 1.2	30.6 ± 1.13	...	...	...	3.22	6.28E−15	1.06E−15	3	−0.32 ± 0.13	1.49E+43
96.....	242.83466	54.58537	956. ± 3.36	630. ± 3.49	428. ± 10.3	378. ± 9.3	474. ± 26	1.2	4.53E−15	8.99E−16	4	1.11 ± 0.09	3.99E+41
97.....	242.78481	54.54735	40.3 ± 0.978	31.8 ± 1.14	...	...	448. ± 23.1	0.60	3.93E−15	7.91E−16	3	−0.64 ± 0.18	1.93E+43
98.....	242.77934	54.59368	8.09 ± 0.855	12.9 ± 1.12	...	...	...	1.77	2.18E−15	6.03E−16	3	−0.13 ± 0.22	4.05E+43
99.....	242.76178	54.49972	9.75 ± 0.832	7.80 ± 1.09	...	...	...	0.58	6.99E−15	1.16E−15	1	−0.15 ± 0.15	3.10E+43
100.....	242.75789	54.64089	49.9 ± 0.863	34.8 ± 0.973	...	18.1 ± 4.05	...	3.31	3.17E−15	7.33E−16	3	−0.11 ± 0.18	1.28E+43

TABLE 2—*Continued*

ID (1)	R.A. (deg) (2)	Decl. (deg) (3)	$S_{3.6}$ (mJy) (4)	$S_{4.5}$ (mJy) (5)	$S_{5.6}$ (mJy) (6)	S_{8} (mJy) (7)	S_{24} (mJy) (8)	d (arcsec) (9)	S_X (10^{-7} W cm^{-2}) (10)	δS_X (10^{-7} W cm^{-2}) (11)	Type (12)	HR (13)	$L_{0.5-8}$ (10^{-7} W) (14)
104.....	242.69458	54.41047	40.3 ± 0.891	34.5 ± 1.18	...	64.8 ± 5.15	...	1.69	1.14E−14	1.46E−15	2	−0.39 ± 0.10	4.41E+43
106.....	242.57269	54.53015	9.10 ± 0.599	13.9 ± 0.802	21.0 ± 4.16	...	198. ± 19.7	1.31	1.38E−15	4.64E−16	1	0.20 ± 0.29	1.89E+43
108.....	242.52039	54.44347	18.7 ± 0.797	20.5 ± 1.12	22.1 ± 4.21	...	...	2.55	6.38E−15	1.07E−15	2	−0.42 ± 0.16	2.80E+43
112.....	242.45084	54.60307	120. ± 1.53	89.4 ± 1.6	80.4 ± 5.99	153. ± 6.25	1303 ± 23.4	0.21	2.41E−15	6.47E−16	2	0.80 ± 0.20	4.99E+42
113.....	242.85968	54.59127	9.67 ± 0.755	17.3 ± 0.822	40.1 ± 4.59	71.0 ± 3.72	62.9 ± 23	0.86	5.14E−15	1.09E−15	1	−0.15 ± 0.16	4.00E+43
114.....	242.76576	54.55086	120. ± 1.78	81.1 ± 2	71.0 ± 5.82	...	...	1.30	2.11E−15	6.23E−16	4	0.05 ± 0.21	2.16E+42
115.....	242.62517	54.40055	115. ± 1.37	91.5 ± 1.57	61.3 ± 5.77	54.0 ± 4.71	169. ± 23.7	4.56	3.84E−15	9.22E−16	4	−0.55 ± 0.18	2.46E+40
116.....	242.59047	54.43574	58.8 ± 1.15	26.0 ± 1.39	...	...	158. ± 23.7	1.30	1.65E−15	5.62E−16	3	0.79 ± 0.18	4.26E+42
117.....	242.57739	54.45892	32.6 ± 1.06	31.8 ± 1.36	...	...	...	2.45	2.42E−15	6.39E−16	3	0.20 ± 0.21	2.12E+43
118.....	242.52217	54.65250	51.1 ± 1.06	31.8 ± 1.42	...	...	118. ± 23.1	2.35	1.73E−15	5.44E−16	2	−0.22 ± 0.26	1.25E+43
119.....	242.47356	54.63194	117. ± 1.43	64.9 ± 1.13	65.1 ± 4.78	...	108. ± 23.2	3.30	1.74E−15	5.47E−16	3	0.72 ± 0.18	3.26E+42
121.....	242.38539	54.57699	25.5 ± 0.801	18.7 ± 0.856	...	...	...	3.65	1.83E−15	5.76E−16	3	0.79 ± 0.14	6.10E+42
124.....	242.88104	54.61811	69.1 ± 1.15	64.8 ± 1.47	86.6 ± 4.92	95.1 ± 5.83	164. ± 23.6	1.66	2.89E−15	8.90E−16	2	−0.38 ± 0.18	9.99E+41
127.....	242.75615	54.50836	...	21.2 ± 1.21	...	...	226. ± 22.1	4.17	2.10E−15	6.83E−16	1	−0.54 ± 0.24	4.64E+42
128.....	242.68021	54.56771	14.8 ± 0.855	15.3 ± 1.18	...	...	110. ± 19	4.8	1.61E−15	5.20E−16	3	−0.37 ± 0.26	1.11E+43
131.....	242.43211	54.64696	15.2 ± 0.959	18.6 ± 1.17	...	...	...	2.10	1.86E−15	5.63E−16	4	−0.04 ± 0.18	2.74E+43
132.....	242.33562	54.51714	62.7 ± 1.26	41.7 ± 1.38	52.1 ± 5.69	80.3 ± 5.87	103. ± 23.5	2.29	2.32E−15	6.70E−16	2	0.00 ± 0.17	4.43E+42
133.....	242.32001	54.46970	17.1 ± 0.948	13.3 ± 1.18	...	...	111. ± 22.3	4.47	5.05E−15	1.07E−15	3	0.25 ± 0.13	2.35E+43
136.....	242.53204	54.64293	237. ± 2.3	145. ± 2.51	98.6 ± 5.96	...	...	1.31	2.17E−15	6.20E−16	4	−0.22 ± 0.24	3.49E+40
139.....	242.42795	54.45282	20.6 ± 0.815	21.5 ± 1.05	64.1 ± 5.19	83.2 ± 4.89	337. ± 22.3	3.89	2.41E−15	6.81E−16	1	−0.34 ± 0.19	4.89E+42
140.....	242.74313	54.64743	10.6 ± 0.713	7.14 ± 1.06	...	...	72.0 ± 24.3	3.13	1.90E−15	5.75E−16	3	−0.66 ± 0.28	2.96E+42
141.....	242.42952	54.69754	37.9 ± 1.05	52.7 ± 1.46	90.2 ± 5.38	71.8 ± 5.85	442. ± 22.1	3.00	2.55E−15	7.72E−16	1	−1.10 ± 0.20	4.29E+42
142.....	242.80632	54.60314	24.0 ± 0.978	28.2 ± 1.31	...	...	435. ± 20.2	1.29	1.97E−15	6.44E−16	1	−0.96 ± 0.25	2.53E+44
143.....	242.41783	54.62019	67.5 ± 1.28	46.5 ± 1.21	...	...	99.3 ± 22.8	3.44	1.52E−15	5.27E−16	2	1.21 ± 0.24	2.55E+42

NOTES.—Col. (1): Identification number as in Manners et al. (2003). Cols. (2) and (3): Right ascension and declination. Col. (4): IRAC flux at 3.6 μm. Col. (5): IRAC flux at 4.5 μm. Col. (6): IRAC flux at 5.6 μm. Col. (7): IRAC flux at 8 μm. Col. (8): MIPS flux at 24 μm. Col. (9): Angular distance of the *Chandra* source to the *Spitzer* identification. Cols. (10) and (11): *Chandra* 0.5–8 keV flux (ergs cm^{-2} s^{-1}) and error. Col. (12): Spectral type ([1] type 1 AGN, [2] type 2 AGN, [3] galaxy, [4] early-type galaxy) based on the optical/IR SED. Col. (13): X-ray hardness ratio. Col. (14): The 0.5–8 keV luminosity. Table 2 is also available in machine-readable form in the electronic edition of the *Astronomical Journal*.

TABLE 3
Details of the Spectral Fits Used with Hyper-*z*

Templates	Spectral Type	Reference
Ell(1.5)	Ell ($t = 1.5$ Gyr)	1
Ell(2)	Ell ($t = 2$ Gyr)	1
Ell(4)	Ell ($t = 4$ Gyr)	1
Ell(13)	Ell ($t = 13$ Gyr)	1
Sa	Sa	1, 2
Sb	Sb	1, 2
Sc	Sc	1, 2
Sd	Sd	1, 2
M100	Sbc + HII	1, 2
NGC 4027	Sdm	3
NGC 4194	Im + HII	3
NGC 6090(SB)	Starburst	1, 2
Sey1	Seyfert 1	3
Sey1.5	Seyfert 1.5	3
Sey2	Seyfert 2	3
Mrk 231	Type 1 AGN+ULIRG	4
IRAS 19254s	Type 2 AGN+ULIRG	4
QSO1	Type 1 QSO	5
LBQS2	Type 1 QSO	5
QSOIR	Type 1 QSO	...[a]
RLFBQS	Type 1 QSO	6
QSO2	Type 2 QSO	7

[a] Same as QSO1 in the optical, IR based on average SED of SWIRE type 1 AGNs (Polletta et al. 2005).

References.—(1) Silva et al. 1998; (2) PAH modified using *ISO* PHT-S spectra; (3) Polletta et al. 2005; (4) Berta et al. 2004; (5) Composite quasar spectra from the Large Bright Quasar Survey (Brotherton et al. 2001); (6) Composite quasar spectra from the FIRST Bright Quasar Survey, Brotherton et al. 2001; (7) FIRST J013435.7−093102 in the optical (Gregg et al. 2002).

classes, while in the optical/near-IR the observations are complemented with a spectrophotometric synthesis code presented in Berta et al. (2004). The library contains spectral templates of all kinds of AGNs, from optical quasars (Brotherton et al. 2001) to red quasars (Gregg et al. 2002), Seyfert 1 to 2 galaxies, and combined quasar/ultraluminous infrared galaxy (ULIRG) sources like the type 1 QSO Mrk 231 and the type 2 quasar/ULIRG Superantennae South (IRAS 19254s; Berta et al. 2003). More information on the spectral fits used with Hyper-*z* is summarized in Table 3.

Figures 5*a*–5*j* display the SEDs and spectral best fits for the 99 extragalactic *Chandra*/SWIRE sources in our sample (three stars are excluded). Data points are plotted for the four IRAC (3.6, 4.5, 5.8, and 8 μm), MIPS 24 μm, U, g', r', i', Z, H, and *Chandra* X-ray bands. Where the sources are detected in the soft (0.5–2 keV) or hard (2–8 keV) *Chandra* images, their fluxes are converted to flux densities at 1 and 5 keV, respectively. Where the *Chandra* source is not detected in both bands, the full band (0.5–8 keV) flux is plotted, corrected to a flux density at 2 keV.

Spectral fits are also shown in the figures, where the best-fitting spectral type is given in the upper right corner of each plot, together with the photometric redshift (value given in parentheses). The spectroscopic redshifts available for 13 sources are reported outside parentheses. Also given in each panel are values for the bolometric luminosities within the observed optical (0.3–3 μm), IR (3–1000 μm), and IRAC (3–10 μm) bands for the best-fitting spectral type.

The spectral fitting was performed only on the optical and IR data points. We have therefore used the best-fitting spectral types to make a prediction for the corresponding X-ray emission in each case. For those spectral types in which the IR emission is dominated by star formation processes, we have calculated the corresponding X-ray emission on the basis of our estimated star formation rate (SFR). Following Franceschini et al. (2003), the SFR is calculated from the bolometric IR luminosity. Given the SFR, the number of high-mass X-ray binaries (HMXBs) can be inferred along with their corresponding 2–10 keV emission. For the case of ULIRGs not dominated by an AGN, it is assumed that all of the X-ray emission comes from HMXBs. In the case of lower luminosity starbursts, a quarter of the 2–10 keV luminosity may be due to HMXBs (the rest being attributable to low-mass X-ray binaries and the quiescent disk). Therefore, our expected 2–10 keV luminosity due to star formation is given by

$$L_{2-10\,\mathrm{keV}} = \left(\frac{1}{f}\right)\frac{L_{\mathrm{IR}}}{2.2\times10^{4}}, \qquad (2)$$

where f ranges from 0.25 to 1 (Franceschini et al. 2003). These expected values of X-ray flux are plotted for each of the starburst-like and "normal galaxy" spectral types. In all cases they are found to underpredict the observed X-ray flux, providing clear evidence for the existence of a hidden AGN in these sources.

For those spectral types in which the IR emission is dominated by the AGN (Seyfert types 1 and 2 and QSOs), we have predicted the associated X-ray emission on the basis of the mean radio-quiet quasar spectrum of Elvis et al. (1994). This is achieved using the ratio of the flux density at 4.5 μm to that at 2 keV; in roughly 2/3 of cases this provides a good prediction of the observed X-ray flux. In the remaining cases the X-ray emission is overpredicted, indicating a component of the IR emission not originating from the AGN.

For the spectral types best fitted by the Mrk 231 template (15 sources in total), the actual X-ray flux of Mrk 231 is plotted as observed by Braito et al. (2004). This strongly underpredicts the observed X-ray fluxes in all cases, consistent with the very low ratio of $S_X/S_{3.6}$ of Mrk 231 indicated in Figure 4 ("D" arrow). Our SWIRE/*Chandra* objects display typical X-ray energy fluxes that are within approximately a decade of those measured in the IR, which demonstrates an AGN dominance in these sources.

3.3. *Source Classification*

Our analysis has found good spectral solutions for a large majority of the sources. Figures 5*a*–5*j* illustrate the quality of the observational spectral coverage and that of our spectral best fits. For a few sources in the figure the photometric redshift is compared with the available spectroscopic measures, with a fairly good agreement between the two.

For seven sources the observational SED coverage is not enough for reliable source characterization. In these cases our adopted classification exploits additional constraints from the X-ray spectrum and the IR to X-ray flux ratios.

We have then grouped sources according to the following four categories: (1) type 1 quasars and AGNs, including 39 objects out of 99 (39%); (2) type 2 quasars and AGNs (23 of 99, 23%); (3) normal and starburst galaxies (33 objects, 33%); and (4) old passive galaxies with purely stellar mid-IR spectra (five galaxies, 5%). We examine in § 3.4 properties of these various classes.

3.4. *A New Diagnostic Diagram Based on Optical/IR SEDs*

We have first attempted to identify a diagnostic diagram able to disentangle various categories of high-redshift active galaxies based on optical/IR colors, which are easily achievable for huge

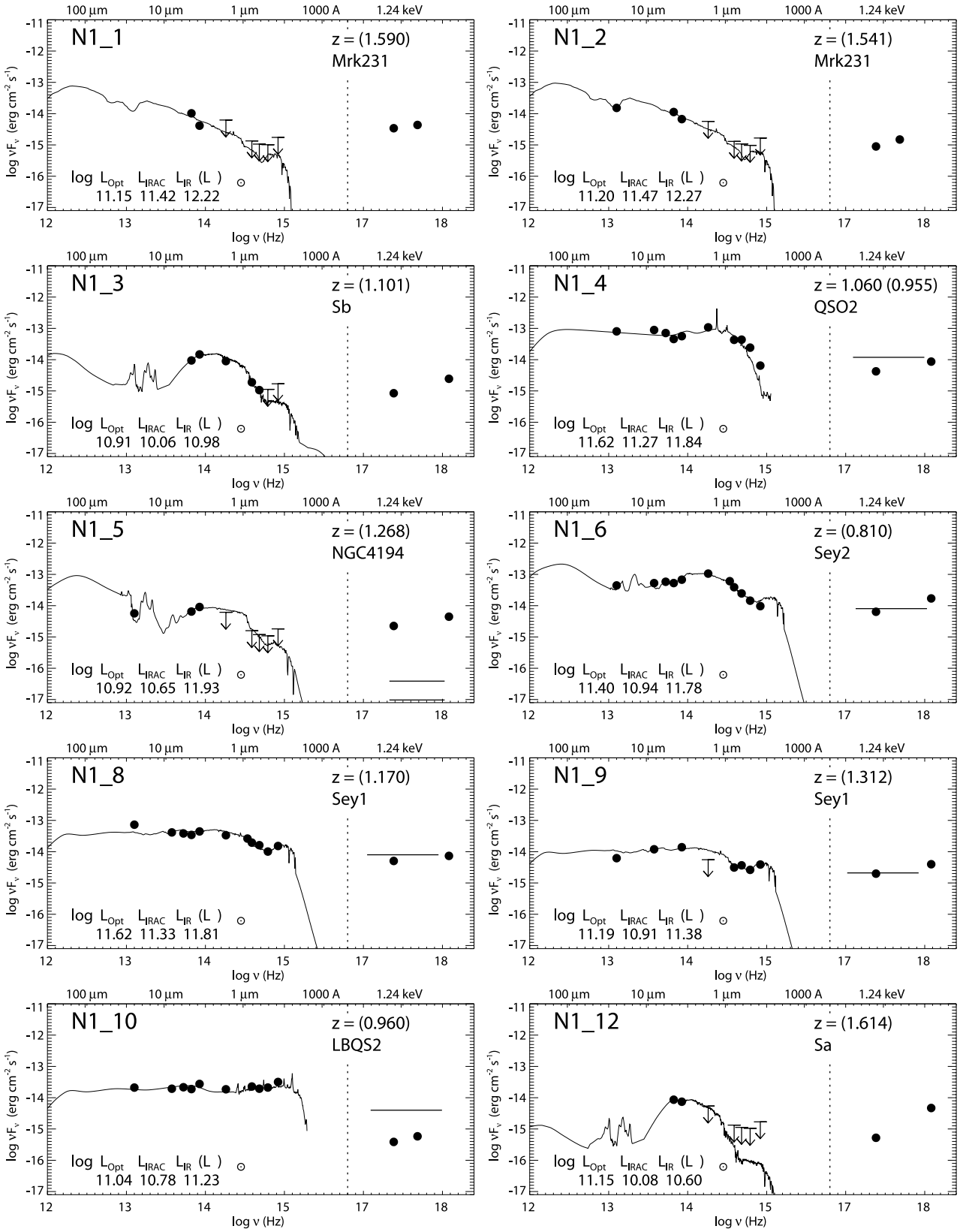

FIG. 5*a*

FIG. 5.—Broadband SEDs and spectral best fits for all 99 *Chandra*/SWIRE sources. The scale on the *x*-axis has been artificially broken between the UV and X-ray bands (*dotted line*) for plot optimization. See text for a more detailed explanation.

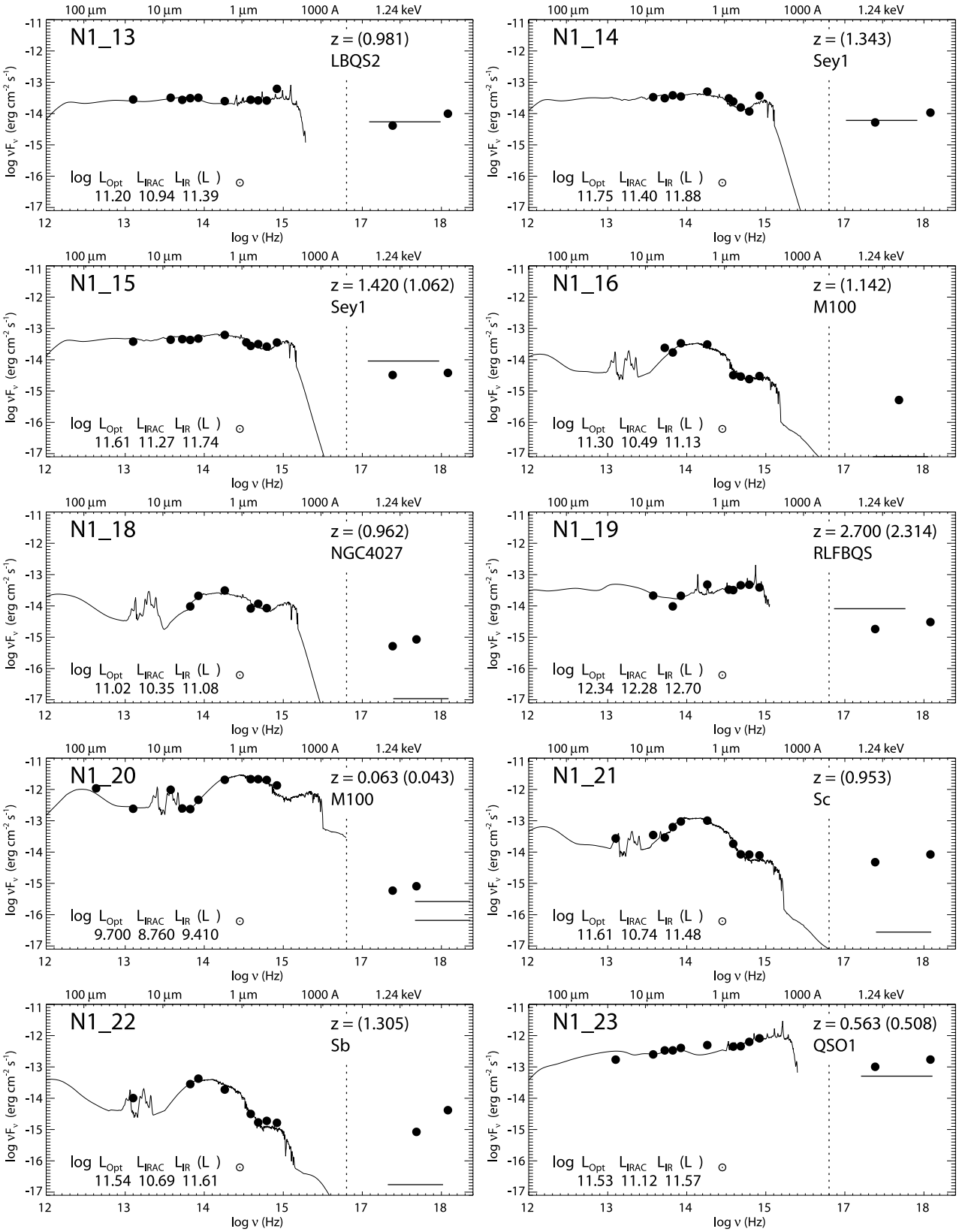
N1_13
z = (0.981)
LBQS2
log L_Opt L_IRAC L_IR (L ⊙)
11.20 10.94 11.39
N1_14
z = (1.343)
Sey1
log L_Opt L_IRAC L_IR (L ⊙)
11.75 11.40 11.88
N1_15
z = 1.420 (1.062)
Sey1
log L_Opt L_IRAC L_IR (L ⊙)
11.61 11.27 11.74
N1_16
z = (1.142)
M100
log L_Opt L_IRAC L_IR (L ⊙)
11.30 10.49 11.13
N1_18
z = (0.962)
NGC4027
log L_Opt L_IRAC L_IR (L ⊙)
11.02 10.35 11.08
N1_19
z = 2.700 (2.314)
RLFBQS
log L_Opt L_IRAC L_IR (L ⊙)
12.34 12.28 12.70
N1_20
z = 0.063 (0.043)
M100
log L_Opt L_IRAC L_IR (L ⊙)
9.700 8.760 9.410
N1_21
z = (0.953)
Sc
log L_Opt L_IRAC L_IR (L ⊙)
11.61 10.74 11.48
N1_22
z = (1.305)
Sb
log L_Opt L_IRAC L_IR (L ⊙)
11.54 10.69 11.61
N1_23
z = 0.563 (0.508)
QSO1
log L_Opt L_IRAC L_IR (L ⊙)
11.53 11.12 11.57
100 μm 10 μm 1 μm 1000 A 1.24 keV
log νF_ν (erg cm^-2 s^-1)
log ν (Hz)

FIG. 5*b*

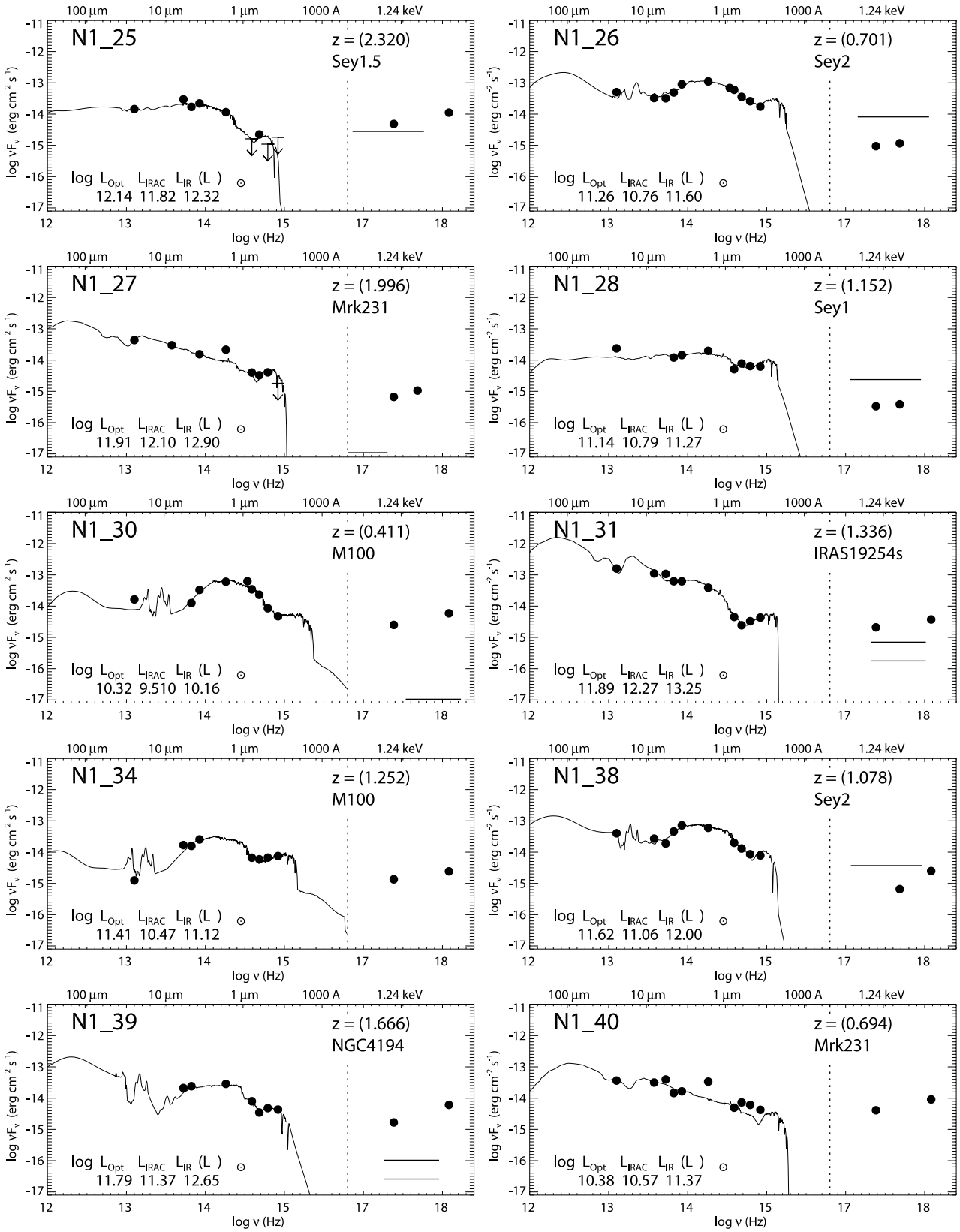
N1_25
z = (2.320)
Sey1.5
log L_Opt L_IRAC L_IR (L ⊙)
12.14 11.82 12.32
N1_26
z = (0.701)
Sey2
log L_Opt L_IRAC L_IR (L ⊙)
11.26 10.76 11.60
N1_27
z = (1.996)
Mrk231
log L_Opt L_IRAC L_IR (L ⊙)
11.91 12.10 12.90
N1_28
z = (1.152)
Sey1
log L_Opt L_IRAC L_IR (L ⊙)
11.14 10.79 11.27
N1_30
z = (0.411)
M100
log L_Opt L_IRAC L_IR (L ⊙)
10.32 9.510 10.16
N1_31
z = (1.336)
IRAS19254s
log L_Opt L_IRAC L_IR (L ⊙)
11.89 12.27 13.25
N1_34
z = (1.252)
M100
log L_Opt L_IRAC L_IR (L ⊙)
11.41 10.47 11.12
N1_38
z = (1.078)
Sey2
log L_Opt L_IRAC L_IR (L ⊙)
11.62 11.06 12.00
N1_39
z = (1.666)
NGC4194
log L_Opt L_IRAC L_IR (L ⊙)
11.79 11.37 12.65
N1_40
z = (0.694)
Mrk231
log L_Opt L_IRAC L_IR (L ⊙)
10.38 10.57 11.37
100 μm 10 μm 1 μm 1000 A 1.24 keV
log νF_ν (erg cm^-2 s^-1)
log ν (Hz)

FIG. 5*c*

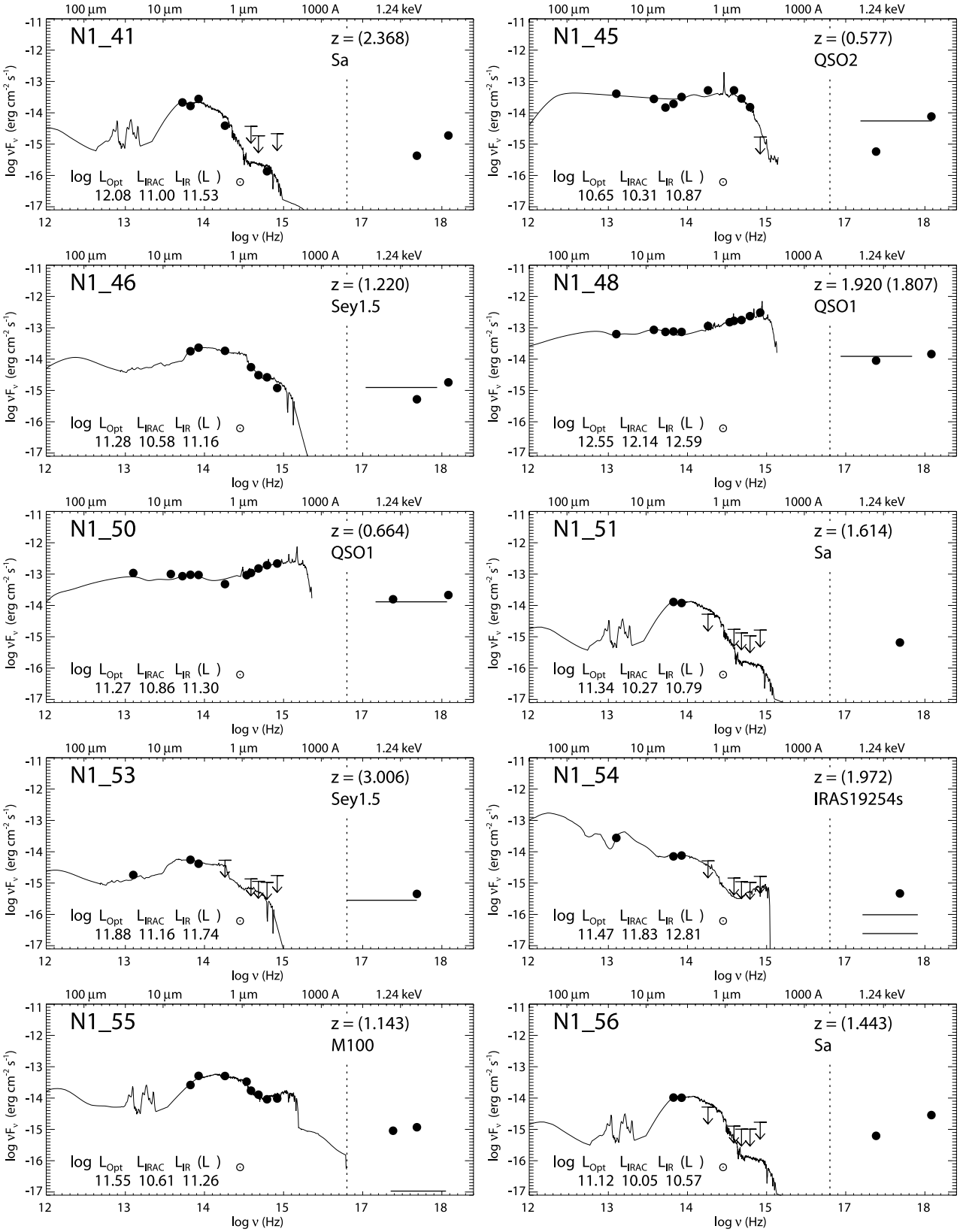
N1_41
z = (2.368)
Sa
log L_Opt L_IRAC L_IR (L ⊙)
12.08 11.00 11.53
N1_45
z = (0.577)
QSO2
log L_Opt L_IRAC L_IR (L ⊙)
10.65 10.31 10.87
N1_46
z = (1.220)
Sey1.5
log L_Opt L_IRAC L_IR (L ⊙)
11.28 10.58 11.16
N1_48
z = 1.920 (1.807)
QSO1
log L_Opt L_IRAC L_IR (L ⊙)
12.55 12.14 12.59
N1_50
z = (0.664)
QSO1
log L_Opt L_IRAC L_IR (L ⊙)
11.27 10.86 11.30
N1_51
z = (1.614)
Sa
log L_Opt L_IRAC L_IR (L ⊙)
11.34 10.27 10.79
N1_53
z = (3.006)
Sey1.5
log L_Opt L_IRAC L_IR (L ⊙)
11.88 11.16 11.74
N1_54
z = (1.972)
IRAS19254s
log L_Opt L_IRAC L_IR (L ⊙)
11.47 11.83 12.81
N1_55
z = (1.143)
M100
log L_Opt L_IRAC L_IR (L ⊙)
11.55 10.61 11.26
N1_56
z = (1.443)
Sa
log L_Opt L_IRAC L_IR (L ⊙)
11.12 10.05 10.57
100 μm 10 μm 1 μm 1000 A 1.24 keV
log νF_ν (erg cm^-2 s^-1)
log ν (Hz)

FIG. 5*d*

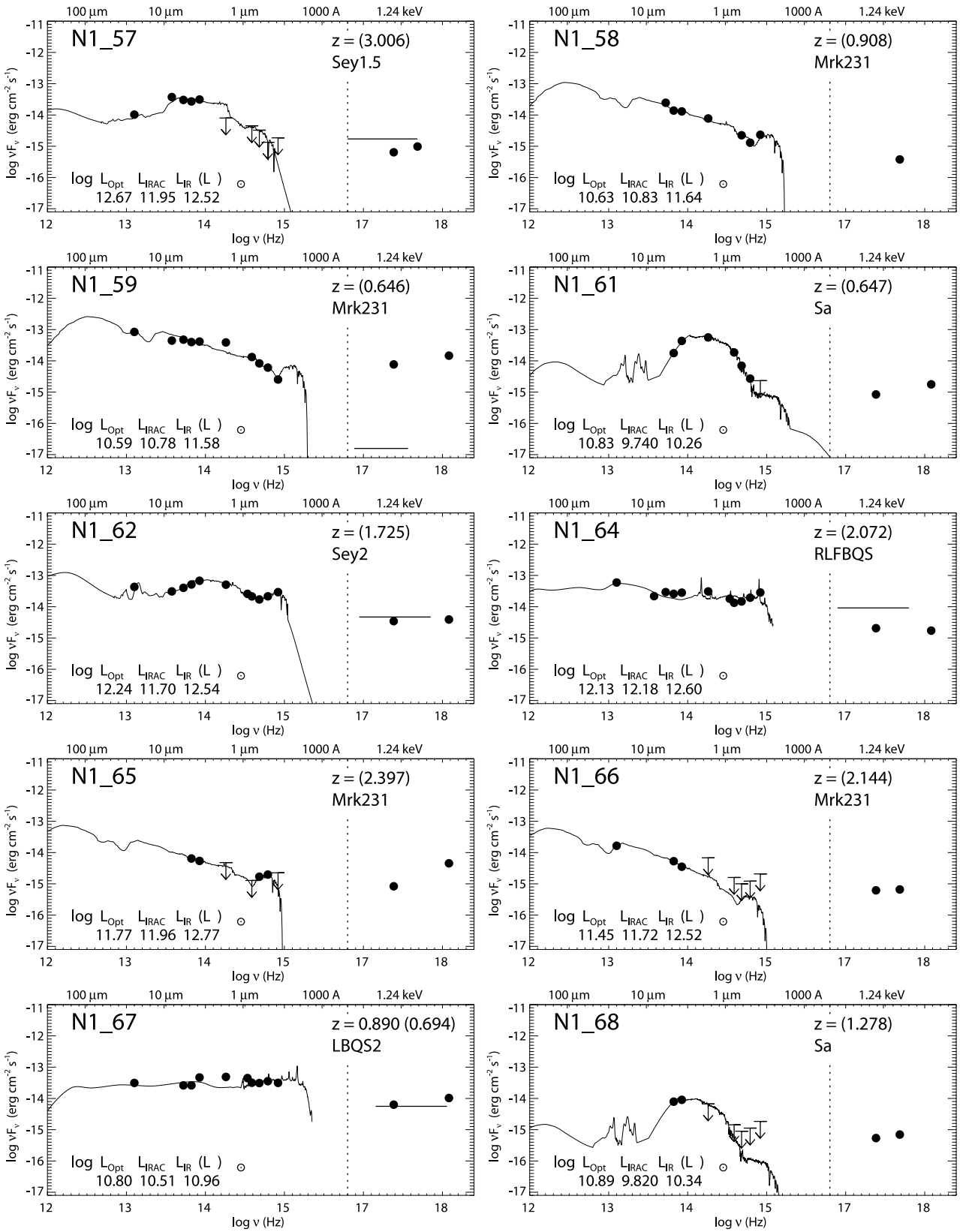
N1_57
z = (3.006)
Sey1.5
log L_Opt L_IRAC L_IR (L ⊙)
12.67 11.95 12.52
N1_58
z = (0.908)
Mrk231
log L_Opt L_IRAC L_IR (L ⊙)
10.63 10.83 11.64
N1_59
z = (0.646)
Mrk231
log L_Opt L_IRAC L_IR (L ⊙)
10.59 10.78 11.58
N1_61
z = (0.647)
Sa
log L_Opt L_IRAC L_IR (L ⊙)
10.83 9.740 10.26
N1_62
z = (1.725)
Sey2
log L_Opt L_IRAC L_IR (L ⊙)
12.24 11.70 12.54
N1_64
z = (2.072)
RLFBQS
log L_Opt L_IRAC L_IR (L ⊙)
12.13 12.18 12.60
N1_65
z = (2.397)
Mrk231
log L_Opt L_IRAC L_IR (L ⊙)
11.77 11.96 12.77
N1_66
z = (2.144)
Mrk231
log L_Opt L_IRAC L_IR (L ⊙)
11.45 11.72 12.52
N1_67
z = 0.890 (0.694)
LBQS2
log L_Opt L_IRAC L_IR (L ⊙)
10.80 10.51 10.96
N1_68
z = (1.278)
Sa
log L_Opt L_IRAC L_IR (L ⊙)
10.89 9.820 10.34
100 μm 10 μm 1 μm 1000 A 1.24 keV
log νF_ν (erg cm^-2 s^-1)
log ν (Hz)

FIG. 5*e*

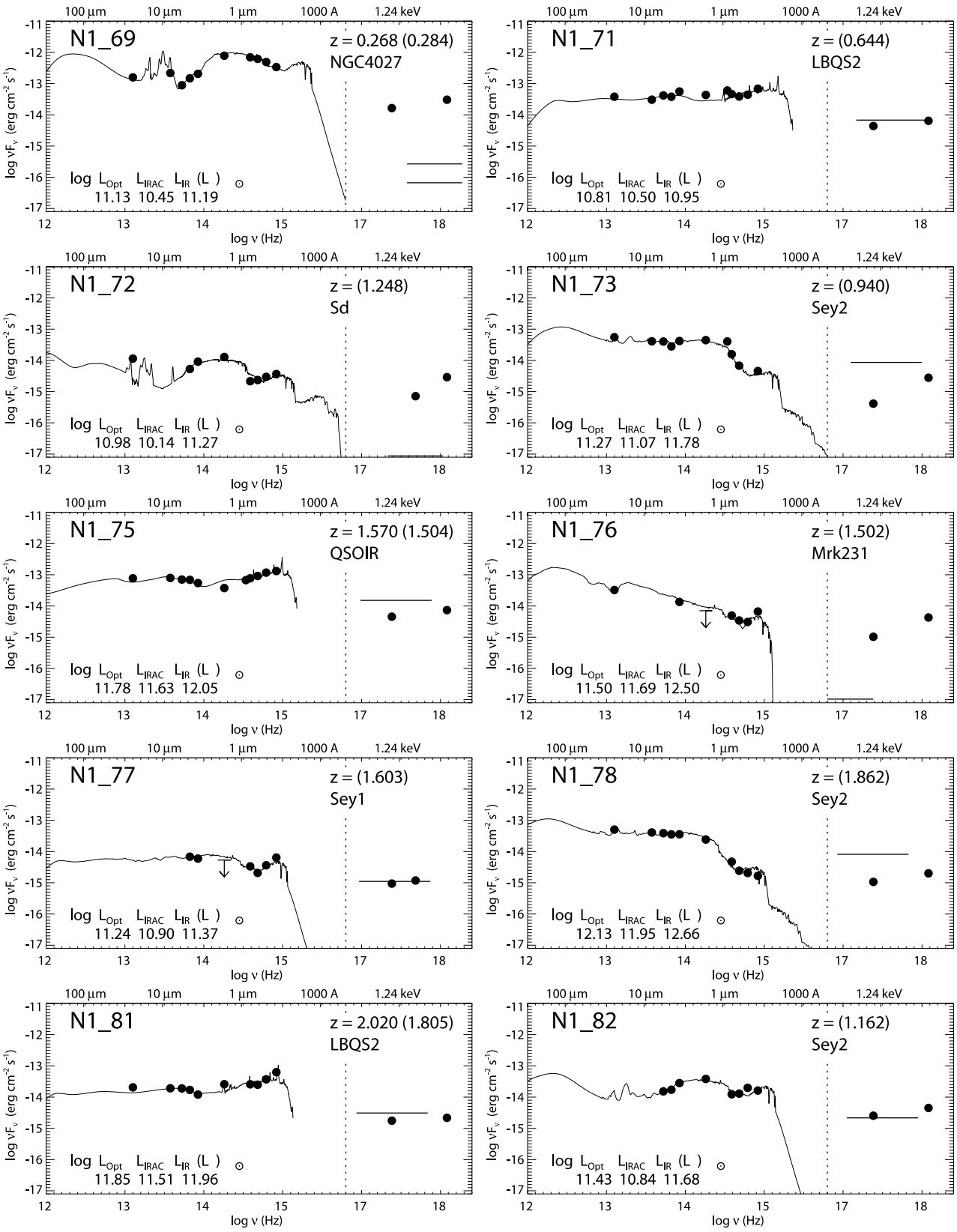
N1_69
z = 0.268 (0.284)
NGC4027
log L_Opt L_IRAC L_IR (L ⊙)
11.13 10.45 11.19
N1_71
z = (0.644)
LBQS2
log L_Opt L_IRAC L_IR (L ⊙)
10.81 10.50 10.95
N1_72
z = (1.248)
Sd
log L_Opt L_IRAC L_IR (L ⊙)
10.98 10.14 11.27
N1_73
z = (0.940)
Sey2
log L_Opt L_IRAC L_IR (L ⊙)
11.27 11.07 11.78
N1_75
z = 1.570 (1.504)
QSOIR
log L_Opt L_IRAC L_IR (L ⊙)
11.78 11.63 12.05
N1_76
z = (1.502)
Mrk231
log L_Opt L_IRAC L_IR (L ⊙)
11.50 11.69 12.50
N1_77
z = (1.603)
Sey1
log L_Opt L_IRAC L_IR (L ⊙)
11.24 10.90 11.37
N1_78
z = (1.862)
Sey2
log L_Opt L_IRAC L_IR (L ⊙)
12.13 11.95 12.66
N1_81
z = 2.020 (1.805)
LBQS2
log L_Opt L_IRAC L_IR (L ⊙)
11.85 11.51 11.96
N1_82
z = (1.162)
Sey2
log L_Opt L_IRAC L_IR (L ⊙)
11.43 10.84 11.68
100 μm 10 μm 1 μm 1000 A 1.24 keV
log νF_ν (erg cm^-2 s^-1)
log ν (Hz)

FIG. 5*f*

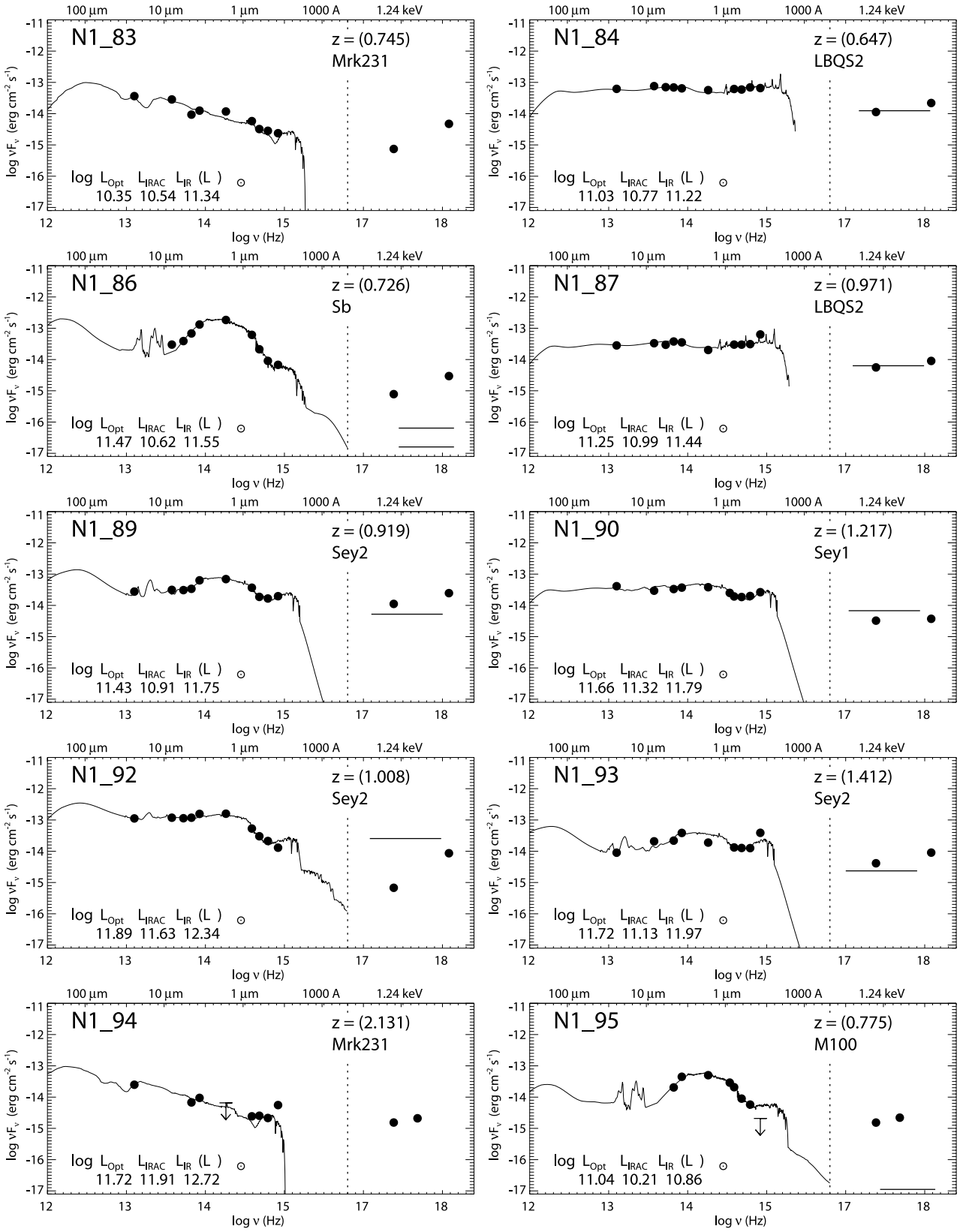
N1_83
z = (0.745)
Mrk231
log L_Opt L_IRAC L_IR (L ⊙)
10.35 10.54 11.34
N1_84
z = (0.647)
LBQS2
log L_Opt L_IRAC L_IR (L ⊙)
11.03 10.77 11.22
N1_86
z = (0.726)
Sb
log L_Opt L_IRAC L_IR (L ⊙)
11.47 10.62 11.55
N1_87
z = (0.971)
LBQS2
log L_Opt L_IRAC L_IR (L ⊙)
11.25 10.99 11.44
N1_89
z = (0.919)
Sey2
log L_Opt L_IRAC L_IR (L ⊙)
11.43 10.91 11.75
N1_90
z = (1.217)
Sey1
log L_Opt L_IRAC L_IR (L ⊙)
11.66 11.32 11.79
N1_92
z = (1.008)
Sey2
log L_Opt L_IRAC L_IR (L ⊙)
11.89 11.63 12.34
N1_93
z = (1.412)
Sey2
log L_Opt L_IRAC L_IR (L ⊙)
11.72 11.13 11.97
N1_94
z = (2.131)
Mrk231
log L_Opt L_IRAC L_IR (L ⊙)
11.72 11.91 12.72
N1_95
z = (0.775)
M100
log L_Opt L_IRAC L_IR (L ⊙)
11.04 10.21 10.86
100 μm 10 μm 1 μm 1000 A 1.24 keV
log νF_ν (erg cm^-2 s^-1)
log ν (Hz)

FIG. 5*g*

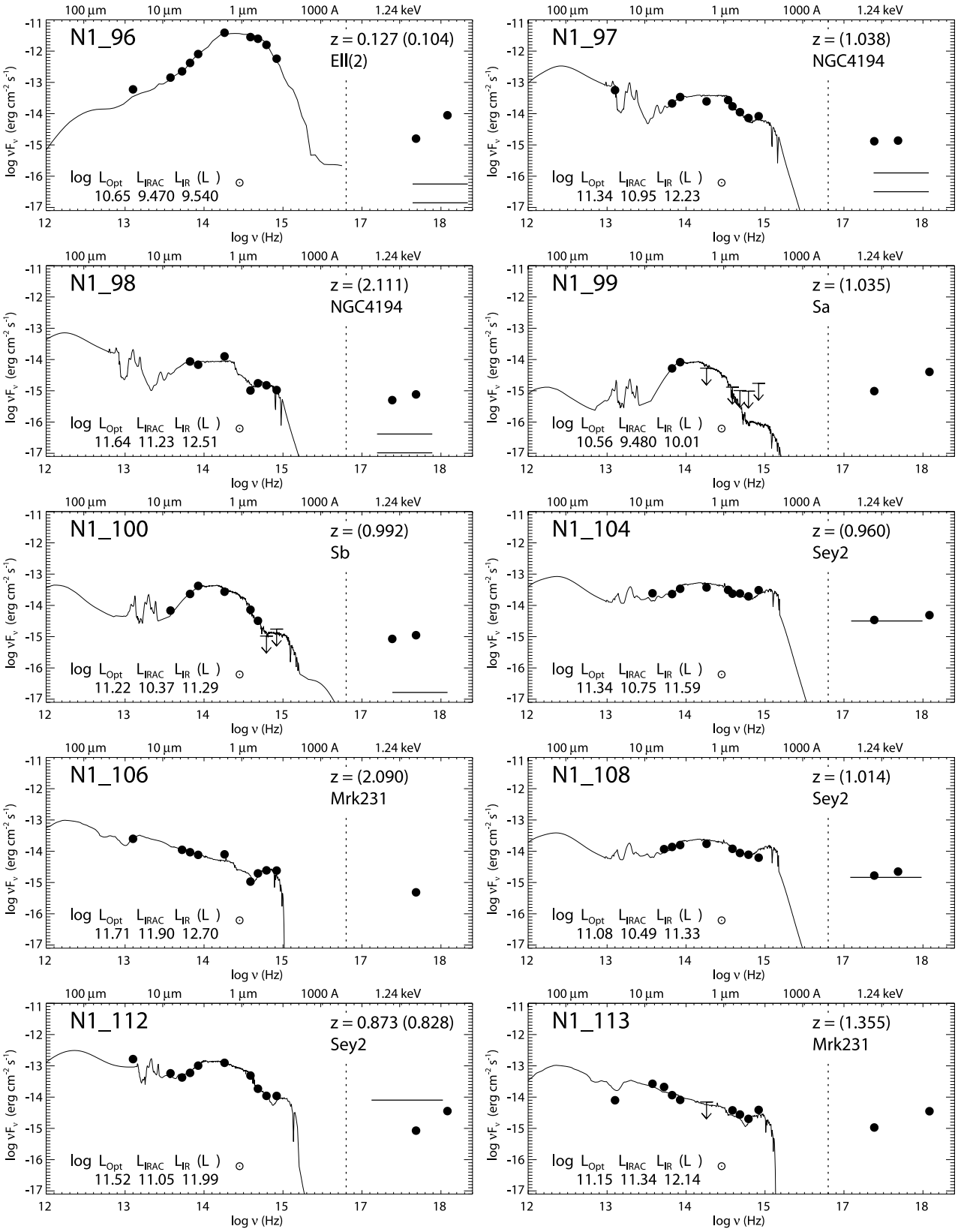
N1_96
z = 0.127 (0.104)
EII(2)
log L_Opt L_IRAC L_IR (L ⊙)
10.65 9.470 9.540
N1_97
z = (1.038)
NGC4194
log L_Opt L_IRAC L_IR (L ⊙)
11.34 10.95 12.23
N1_98
z = (2.111)
NGC4194
log L_Opt L_IRAC L_IR (L ⊙)
11.64 11.23 12.51
N1_99
z = (1.035)
Sa
log L_Opt L_IRAC L_IR (L ⊙)
10.56 9.480 10.01
N1_100
z = (0.992)
Sb
log L_Opt L_IRAC L_IR (L ⊙)
11.22 10.37 11.29
N1_104
z = (0.960)
Sey2
log L_Opt L_IRAC L_IR (L ⊙)
11.34 10.75 11.59
N1_106
z = (2.090)
Mrk231
log L_Opt L_IRAC L_IR (L ⊙)
11.71 11.90 12.70
N1_108
z = (1.014)
Sey2
log L_Opt L_IRAC L_IR (L ⊙)
11.08 10.49 11.33
N1_112
z = 0.873 (0.828)
Sey2
log L_Opt L_IRAC L_IR (L ⊙)
11.52 11.05 11.99
N1_113
z = (1.355)
Mrk231
log L_Opt L_IRAC L_IR (L ⊙)
11.15 11.34 12.14
100 μm 10 μm 1 μm 1000 A 1.24 keV
log νF_ν (erg cm^-2 s^-1)
log ν (Hz)

FIG. 5*h*

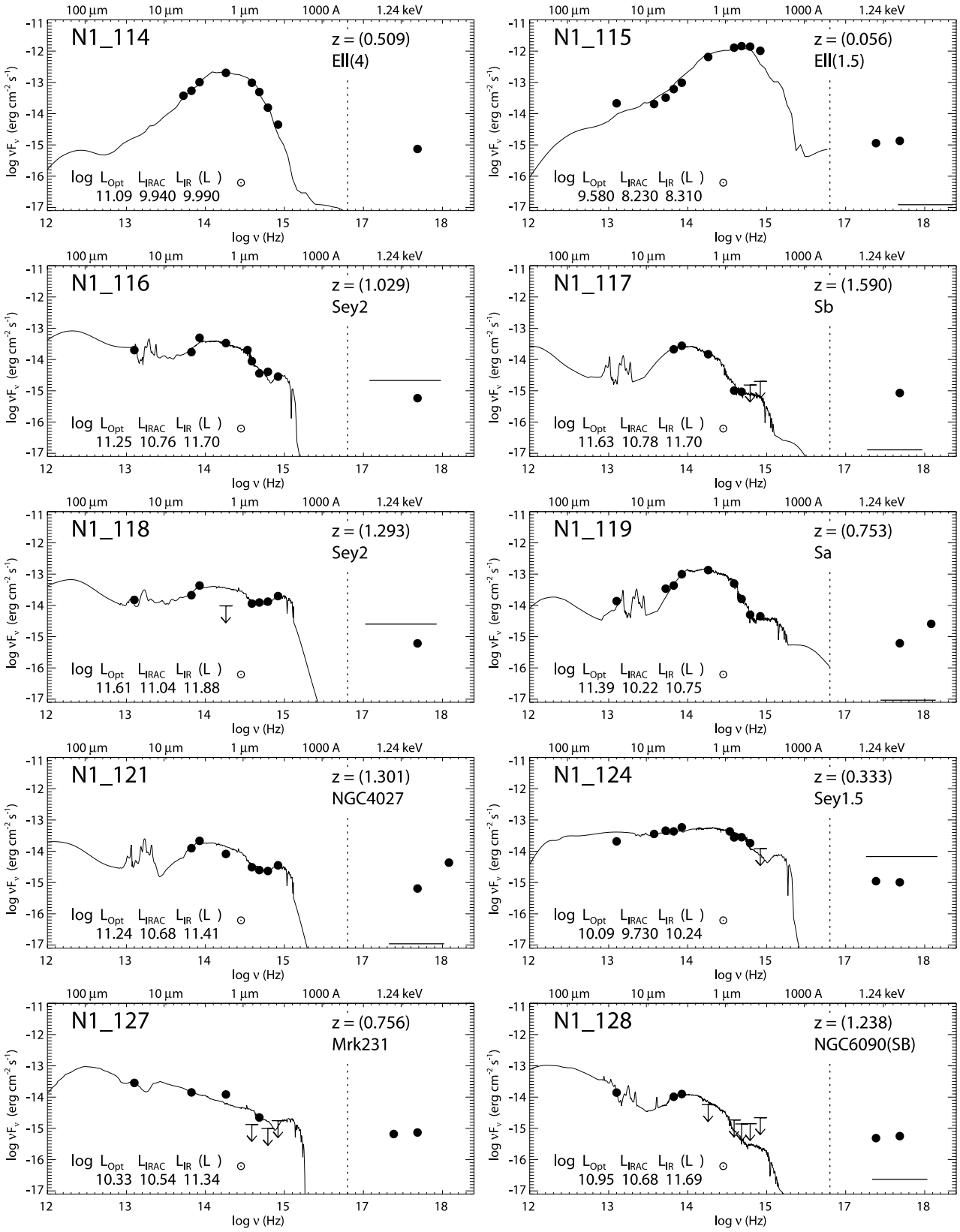
N1_114
z = (0.509)
EII(4)
log L_Opt L_IRAC L_IR (L ⊙)
11.09 9.940 9.990
N1_115
z = (0.056)
EII(1.5)
log L_Opt L_IRAC L_IR (L ⊙)
9.580 8.230 8.310
N1_116
z = (1.029)
Sey2
log L_Opt L_IRAC L_IR (L ⊙)
11.25 10.76 11.70
N1_117
z = (1.590)
Sb
log L_Opt L_IRAC L_IR (L ⊙)
11.63 10.78 11.70
N1_118
z = (1.293)
Sey2
log L_Opt L_IRAC L_IR (L ⊙)
11.61 11.04 11.88
N1_119
z = (0.753)
Sa
log L_Opt L_IRAC L_IR (L ⊙)
11.39 10.22 10.75
N1_121
z = (1.301)
NGC4027
log L_Opt L_IRAC L_IR (L ⊙)
11.24 10.68 11.41
N1_124
z = (0.333)
Sey1.5
log L_Opt L_IRAC L_IR (L ⊙)
10.09 9.730 10.24
N1_127
z = (0.756)
Mrk231
log L_Opt L_IRAC L_IR (L ⊙)
10.33 10.54 11.34
N1_128
z = (1.238)
NGC6090(SB)
log L_Opt L_IRAC L_IR (L ⊙)
10.95 10.68 11.69
100 μm 10 μm 1 μm 1000 A 1.24 keV
log νF_ν (erg cm^-2 s^-1)
log ν (Hz)

FIG. 5*i*

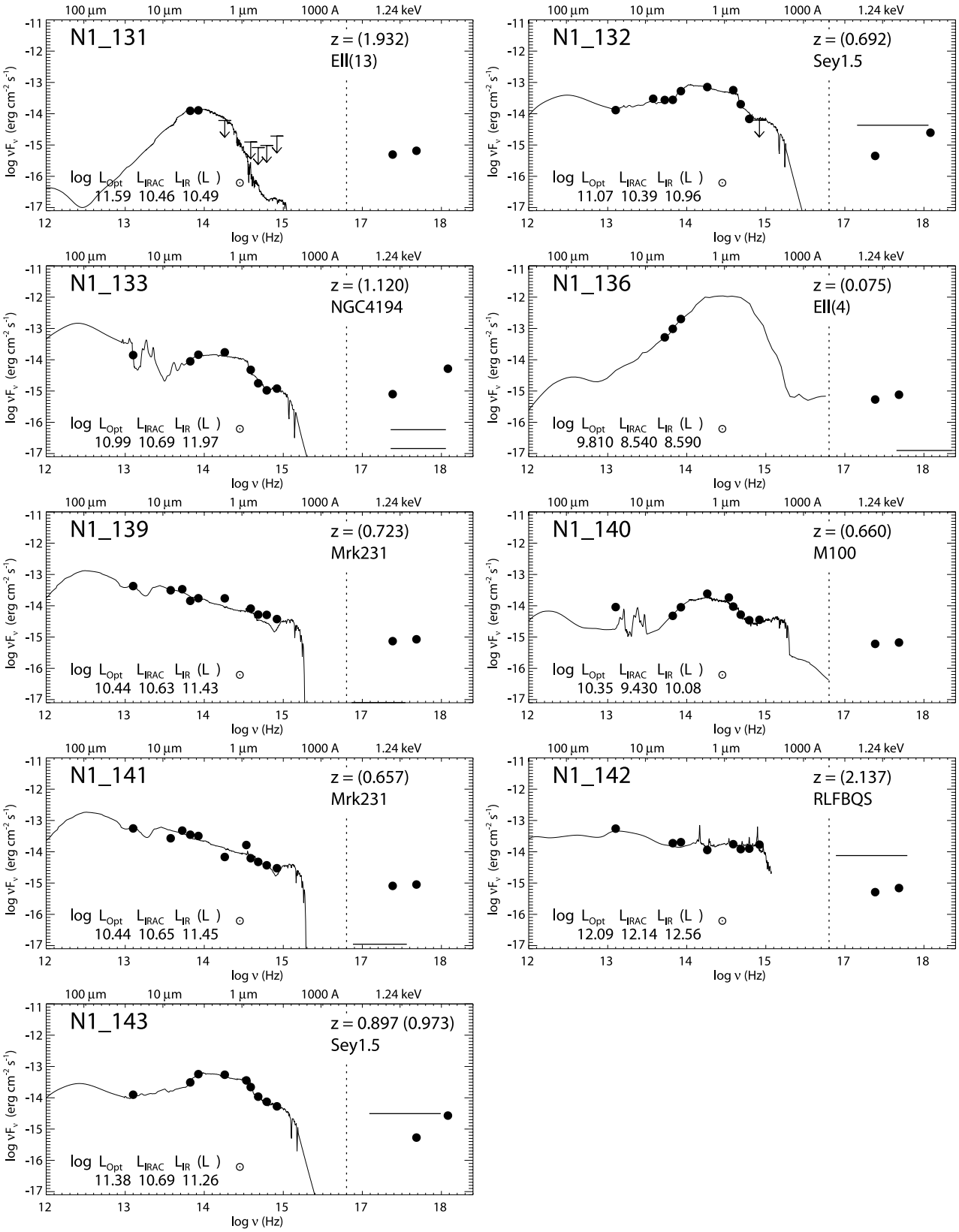
N1_131
z = (1.932)
EII(13)
log L_Opt L_IRAC L_IR (L ⊙)
11.59 10.46 10.49
N1_132
z = (0.692)
Sey1.5
log L_Opt L_IRAC L_IR (L ⊙)
11.07 10.39 10.96
N1_133
z = (1.120)
NGC4194
log L_Opt L_IRAC L_IR (L ⊙)
10.99 10.69 11.97
N1_136
z = (0.075)
EII(4)
log L_Opt L_IRAC L_IR (L ⊙)
9.810 8.540 8.590
N1_139
z = (0.723)
Mrk231
log L_Opt L_IRAC L_IR (L ⊙)
10.44 10.63 11.43
N1_140
z = (0.660)
M100
log L_Opt L_IRAC L_IR (L ⊙)
10.35 9.430 10.08
N1_141
z = (0.657)
Mrk231
log L_Opt L_IRAC L_IR (L ⊙)
10.44 10.65 11.45
N1_142
z = (2.137)
RLFBQS
log L_Opt L_IRAC L_IR (L ⊙)
12.09 12.14 12.56
N1_143
z = 0.897 (0.973)
Sey1.5
log L_Opt L_IRAC L_IR (L ⊙)
11.38 10.69 11.26
100 μm 10 μm 1 μm 1000 A 1.24 keV
log νF_ν (erg cm^-2 s^-1)
log ν (Hz)

FIG. 5*j*

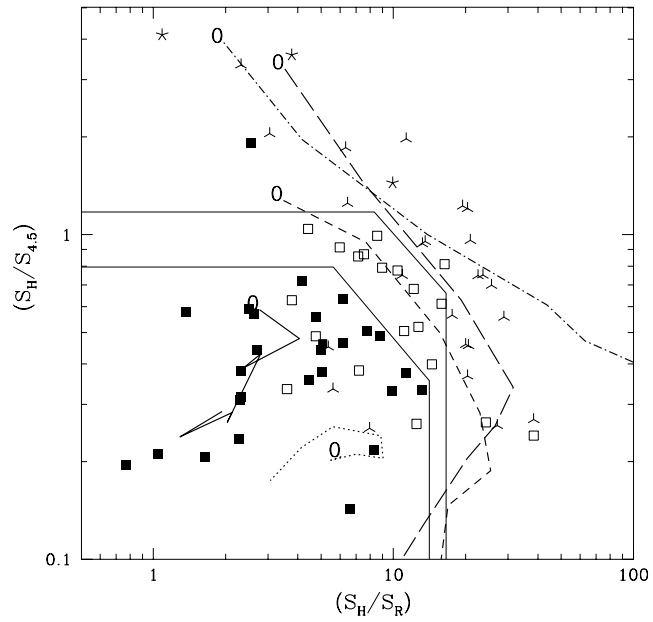

FIG. 6.—Color-color plot with $S_H/S_{4.5}$ vs. S_H/S_R. Here S_H and S_R are the flux densities in the near-IR H band and the optical R band. Four source categories are reported here: type 1 quasars and AGNs (*filled squares*), type 2 AGNs (*open squares*), normal spirals and starbursts (*three-point stars*), and early-type galaxies (*five-point stars*). These four categories preferentially populate different regions of the diagram, which are indicated by the two thin solid lines. The lower line is defined by the two points on the graph at $(10^{0.75}, 10^{-0.1})$ and $(10^{1.15}, 10^{-0.45})$. The upper line is defined by the two points at $(10^{0.92}, 10^{0.07})$ and $(10^{1.22}, 10^{-0.18})$. The other thicker lines show the expected evolution of colors as a function of redshift for various spectral templates: *dot-dashed line*, elliptical galaxy; *long-dashed line*, Sb spiral/starburst; *short-dashed line*, Seyfert 2; *solid line*, Seyfert 1 or quasar; *dotted line*, Mrk 231. The color for $z = 0$ is the point marked with "0"; then lines are drawn from here to the points corresponding to $z = 0.5$, 1, 1.5, 2, 2.5, 3, and 3.5.

numbers of sources from combined deep surveys with *Spitzer* and optical ground-based telescopes.

We have found that a maximum segregation of our four categories is obtained by combining the H-band to 4.5 μm color against the H-band ($\lambda_{\rm eff} = 1.7$ μm) to R-band magnitudes. As illustrated in Figure 6, our three classes tend to populate different regions of the color-color diagram, which are delimited by the two thin solid lines. In this plot, type 1 AGNs occupy the lower left corner, corresponding to sources with excess 4.5 μm emission (of quasar origin) but blue or very blue optical to H-band spectra. With respect to these, type 2 AGNs appear to be shifted toward an excess in the 4.5 μm and H-band fluxes. Finally, galaxies classified as normal (i.e., starbursts or quiescent disks) tend to occupy a quite complementary domain of the graph with respect to the previous two: if such galaxies are relatively blue in the H to optical color, they show no mid-IR excess (*upper left corner*); if they are red in the optical, they are also red in the near- to mid-IR.

This behavior is easily understandable on the basis of what we expect the typical source SEDs to be and what we anticipated in § 3.3: type 1 quasars have "concave" SEDs with a minimum in the rest frame around 1 μm. Normal galaxies have a maximum around 1 μm, being redshifted toward longer wavelengths, which is a spectral behavior quite complementary to that of quasars. Type 2 AGNs have spectra similar to those of type 1 AGNs, but with an excess in the H band corresponding to the emergent contribution of the host galaxy. Another feature of type 2 AGNs is that they lack the UV excess of type 1 objects and avoid the region of very blue H/R colors (low values of the S_H/S_R ratio).

The fluxes in the H band and IRAC 4.5 μm band are particularly critical for separating the contributions of the host galaxy from that of the nuclear AGNs. However, our result here indicates that only a two-color diagnostic can work, whereas a single-color criterion (e.g., that based on the $S_H/S_{4.5}$ color) is subject to high degeneracy.

Note that the diagram of Figure 6 seems to work for sources within our properly sampled redshift interval, i.e., up to $z \simeq 2.5$, but with poor statistics above $z = 1.5$. A more extensive data set will be needed to prove whether similar diagnostics might work on a wider redshift interval.

We have attempted to verify the effect of the source redshift in this plot in a modelistic way by overplotting lines corresponding to the expected evolution of colors as a function of redshift for various different spectral templates. For each of the overplotted lines in Figure 6, the color for redshift $z = 0$ corresponds to the start point marked with "0." Then lines are drawn from here to the points corresponding to $z = 0.5$, 1, 1.5, 2, 2.5, 3, and finally 3.5. The dot-dashed line is for an elliptical galaxy template, the long-dashed line is for an Sb spiral/starburst, the short-dashed line is for a Seyfert 2 galaxy, the solid line is for a type 1 Seyfert galaxy or quasar, and finally the dotted line is for the Mrk 231 spectral template. It is evident that while for typical type 1 AGNs (the latter two) the evolution of colors with redshift is very modest, and they keep well within the lower left quadrant for any z (because of the featureless broadband spectra), strong color evolution is expected for all other categories. In particular, the $H/R/4.5$ μm colors migrate from the upper left to lower right at increasing redshifts.

In any case, the expected colors remain within the boundaries for the various categories up to $z = 3.5$, except for type 2 AGNs and starbursts, for which they tend to become confused at $z > 1.5$–2.

3.5. *Flux Correlations and Color-Color Plots*

The relation between X-ray and mid-IR fluxes is an important one for constraining the distribution of the circumnuclear absorbing medium and eventually for testing the unification scheme. Various correlation analyses have been published (Maiolino et al. 1995; Krabbe et al. 2001; Lutz et al. 2004), not all of them finding unequivocal results, however.

We have performed an X-ray to IR flux correlation study by exploiting our large sample and extensive IR coverage. We report in Figure 7 plots of the X-ray flux densities at 4 keV (based on *Chandra* fluxes in the total 0.5–8 keV band) versus those in the IRAC and MIPS 24 μm bands for our various classes of sources.

X-ray and mid-IR fluxes appear to be significantly correlated only for type 1 quasars and AGNs. The Spearman correlation coefficient for the 3.6, 4.5, and 8 μm IRAC fluxes and the MIPS 24 μm flux are C.C. = 0.70, 0.69, 0.81, and 0.62, respectively; the tightest correlation is then with the 8 μm flux, while the one between the X-ray and far-IR 24 μm fluxes is less significant.

For the type 2 AGNs and for normal galaxies and starbursts (our sources in categories 3 and 4) the correlations are much poorer (Spearman C.C. = 0.02, 0.16, 0.06, and 0.2, in the same order, and C.C. = 0.17, 0.16, 0.17, and 0.40, respectively). Perhaps surprisingly, none of these results depend significantly on the X-ray bandwidth, soft or hard, adopted for the comparison. Although not statistically significant, it is interesting to note that the scatter in the X-ray to IR correlation for type 1 AGNs, and even more so for other sources, increases at the lower fluxes. This seems to be an intrinsic effect, not due to the

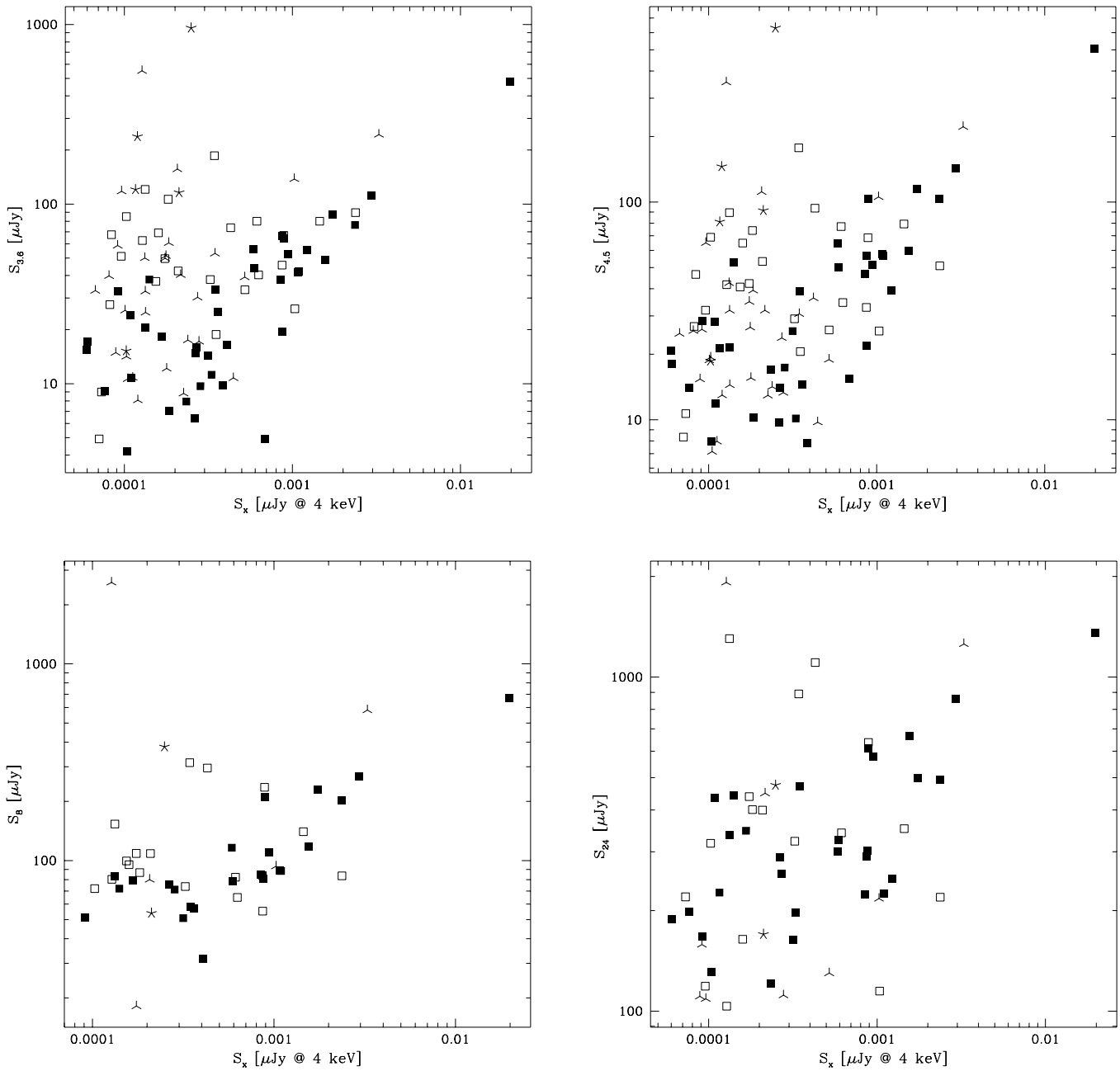

FIG. 7.—Relation between the IRAC and MIPS 24 μm flux densities (in μJy) and the X-ray flux densities at 4 keV (based on *Chandra* fluxes in the total 0.5–8 keV band). In all panels filled squares are type 1 quasars, open squares are type 2 AGNs, three-point stars are spirals and starbursts, and five-point stars are early-type galaxies. The different panels show the correlation with the 3.6 μm (*top left*), 4.5 μm (*top right*), and 8 μm (*top right*) IRAC and 24 μm MIPS (*bottom right*) fluxes.

increased photometric uncertainties at the lower fluxes, which are lower than the observed scatter.

This may support the case that for type 1 AGNs, the IR and X-ray emissions originate from a single dominant physical process, i.e., energy production by gravitational accretion. Furthermore, absorption effects in the dust torus due to atomic photoelectric effects and dust extinction should be unimportant. This may be in keeping with the notions that (1) in type 1 AGNs the contribution of star formation to the energy production is irrelevant compared with the QSO emission itself, (2) the line of sight is not intersecting large column densities of absorbing material, and (3) the dust distribution covers only a fraction of the ionizing photons emitted by the central power source (see § 3.9 about this point).

All this is evidently not true for the other classes of sources. As recently discussed in Lutz et al. (2004), the large contribution of star formation, particularly to the mid- and far-IR emissions, is likely to be responsible for increasing the scatter going from the type 1 to type 2 AGN population. Eventually, the lack of apparent correlation between X-ray and IR emission in the X-ray subsample identified with normal or purely starburst galaxies in the optical/IR shows that the two emissions may come from independent physical processes (quasar nuclear activity and stellar emission, either direct or dust reprocessed).

Finally, an attempt to combine an optical/IR color criterion with the ratio of the IR to X-ray flux is reported in Figure 8. Here the ratio of the X-ray to IR flux is compared with the IRAC channel 2 to *H*-band color. Type 1 quasars cluster around the

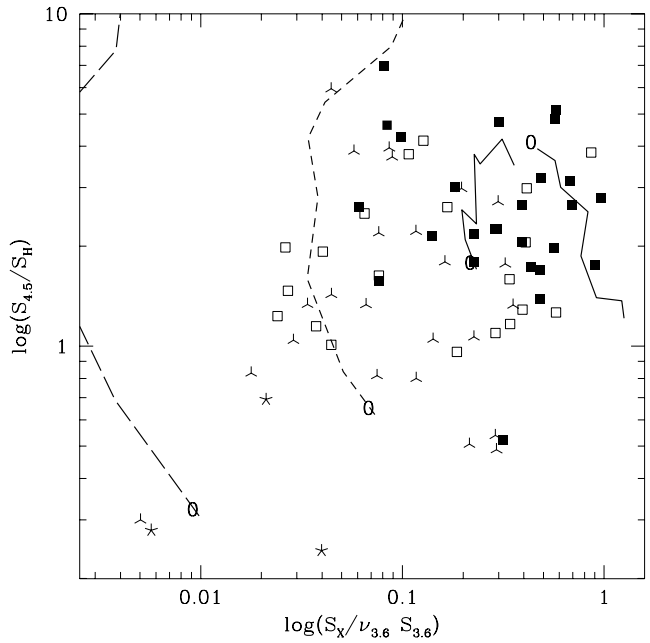

FIG. 8.—IRAC 4.5 μm to H-band colors vs. the ratios of the X-ray to IR fluxes. Here S_X is the flux in the total 0.5–8 keV band, and $\nu_{3.6} S_{3.6}$ is the IRAC channel 1 band flux. Symbols are as in Fig. 6. The lines are the predicted broadband colors as a function of z; the color for $z = 0$ corresponds to the point marked with "0," and lines are drawn from here to points corresponding to $z = 0.5$, 1, 1.5, 2, 2.5, 3, and 3.5. From right to left, the lines are type 1 quasar and Seyfert 1 (*two solid lines*), Seyfert 2 (*short-dashed line*), and Sb spiral/starburst (*long-dashed line*).

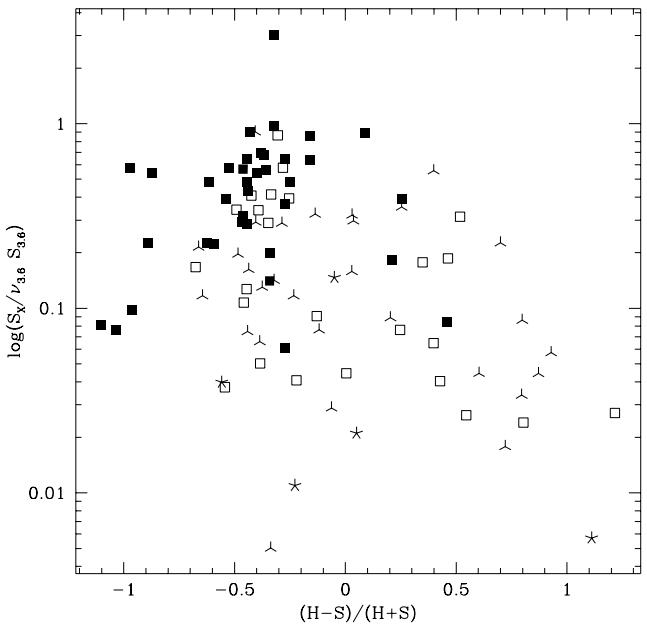

FIG. 9.—X-ray hardness ratio vs. X-ray to IR flux ratio. The hardness ratio HR is defined as $(H - S)/(H + S)$, where H and S are the net X-ray counts in the hard (2.0–8.0 keV) and soft (0.5–2.0 keV) bands. Here S_X is the usual total 0.5–8 keV flux. Symbols are as in Fig. 6.

upper right corner (high X-ray and mid-IR emissions), while type 2 AGNs and sources with starburst optical/IR colors scatter over a much wider region.

In the same figure we report the predicted broadband colors for spectral templates as a function of the source redshift. As in Figure 6, for each line the color for redshift $z = 0$ corresponds to the point marked with "0," and lines are drawn from here to the points corresponding to $z = 0.5$, 1, 1.5, 2, 2.5, 3, and 3.5. Going from the right to the left, the two solid lines are for a type 1 quasar and a Seyfert 1 template, the short-dashed line is for a Seyfert 2, and the long-dashed line is for an Sb spiral/starburst. The X-ray to IR flux ratios of the templates come from observations of local sources (see §§ 3.1 and 3.2). This confirms that for type 1 objects the evolution of flux ratios is very moderate, while it is more pronounced for type 2 objects and starbursts.

An important point emerging from Figure 8 is that the X-ray to IRAC flux ratios $S_X/\nu_{3.6} S_{3.6}$ of our source sample are, almost without exception, inconsistent with X-ray emission due to a starburst (whose z-dependent path in this color-color diagram should be close to the long-dashed line in the far left). This agrees well with the results of Figure 4.

3.6. *X-Ray Hardness Ratio Analysis*

The spectral information contained in our deep *Chandra* X-ray survey provides additional value for source characterization. Given the limited depth and photon counts, the X-ray spectral data were summarized in the usual form of a broadband hardness ratio HR. This was defined as $\mathrm{HR} = (H - S)/(H + S)$, where H and S are the background-subtracted X-ray counts in the hard (2.0–8.0 keV) and soft (0.5–2.0 keV) bands, respectively. Full details on the HR calculation can be found in Manners et al. (2003).

Figure 9 plots such a hardness ratio against the X-ray to IR flux ratio. A first obvious effect is the clustering of type 1 quasars and AGNs around values of $\mathrm{HR} \simeq -0.5$ and values of the X-ray to IR flux ratio from 0.3 to 1. Such values of HR correspond to the classical $\alpha_X = 0.7$ unabsorbed spectrum.

Type 2 AGNs tend to spread out of the canonical AGN 1 region and to display significantly harder X-ray spectra and a lower X-ray emissivity. Both these effects are easily interpreted as being due to X-ray photoelectric absorption. A similar depression of the X-ray emissivity is apparent in Figure 7, correlating the IRAC channel 1 and total X-ray fluxes. The population of optically classified normal galaxies and starbursts displays an even farther spread out of the type 1 region.

What is interesting to note about this and Figure 8, however, is that a hardening of the X-ray spectrum and a decrease of the mid-IR AGN excess do not correspond to a dramatic decrease of the source X-ray emissivity, as might be expected in the presence of strong absorption in either X-rays or the IR or because of a change in the source population: with few exceptions, the values of the X-ray to IR flux ratio span a range not larger than a factor of 30 all together.

3.7. *Redshift and Luminosity Distributions*

We now undertake the more uncertain task of exploiting the information on cosmic distances for our combined *Chandra*/SWIRE sample, mostly based on the photometric redshift technique. Until we acquire a more systematic spectroscopic coverage for this sample, such information on redshifts should be taken in a statistical sense rather than as values for individual sources. This is particularly the case for the featureless type 1 AGNs.

We report in Figure 10 the photometric redshift distributions for our sample sources split into three different classes: type 1 AGNs (*shaded histogram*), type 2 AGNs (*dotted histogram*), and normal galaxies and starbursts (our previous classes 3 and 4, *dashed histogram*). The total distribution is reported as a solid line. It is evident that our source sampling mainly detects galaxies

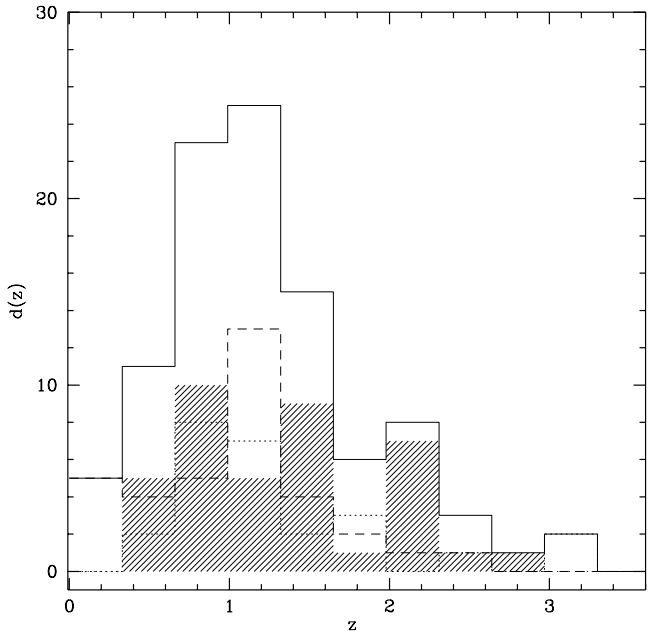

FIG. 10.—Redshift distributions for 99 sources detected by *Chandra* in ELAIS N1 and identified with galaxies or AGNs (three stars are excluded). Three classes of sources are shown: type 1 AGNs (*shaded histogram*), type 2 AGNs (*dotted histogram*), and normal galaxies and starbursts (our previous classes 3 and 4, *dashed histogram*).

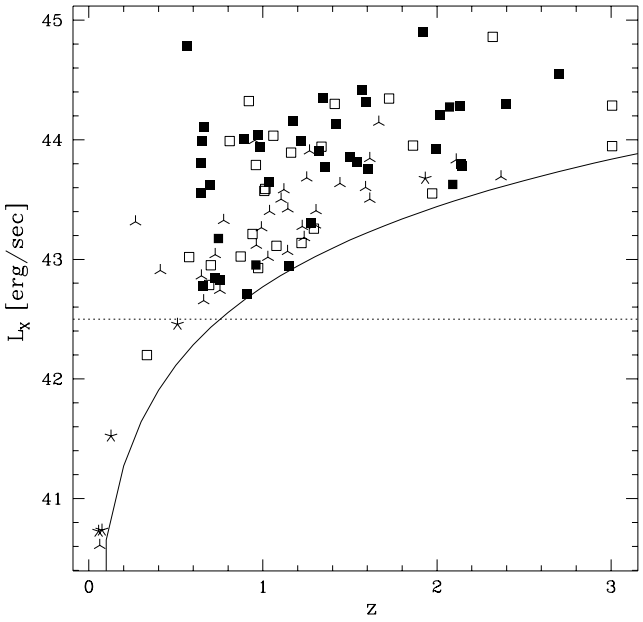

FIG. 11.—Distribution of rest-frame 0.5–8 keV X-ray luminosity and redshift for 99 sources detected by *Chandra* in ELAIS N1. The bulk of redshifts are photometric and are to be taken as only indicative for type 1 AGNs. Source symbols are as in Fig. 6. The dotted line marks the upper boundary of the X-ray luminosity produced by an ultraluminous starburst. The solid line shows the $S_X = 10^{-15}$ ergs cm^{-2} s^{-1} observational flux limit.

and AGNs between $z \sim 0.5$ and $z \sim 1.5$, with a maximum at $z = 1$ and a fairly sustained tail up to $z = 2.5$.

This distribution is interestingly similar to that reported by Zheng et al. (2004), which comes from an optical spectroscopic survey of the deep *Chandra* survey in the *Chandra* Deep Field South (CDFS), complemented with a photometric redshift analysis similar to ours. In the CDFS the observed z-distribution shows a narrow peak at $z = 0.6$, which we do not observe, probably due to a large clustering overdensity in their sample. Compared to that of Zheng et al., a substantial advantage of our analysis is in the very extensive coverage of the mid- and far-IR bands that contains important diagnostic information and brings improved capabilities for redshift determination.

It is important to note that our sample is very representative of the sources of the XRB, if we consider that it includes 84% of the *Chandra* X-ray sample complete to $S_{0.5-8\,\mathrm{keV}} \simeq 2 \times 10^{-15}$ ergs cm^{-2} s^{-1}; sources detected at this limit contribute roughly 60% of the XRB (Manners et al. 2003; see also Hasinger et al. 2001; Brandt et al. 2001; Giacconi et al. 2001). Our present results confirm earlier reported evidence (Hasinger 2003; Barger et al. 2003; Szokoly et al. 2004; Gilli et al. 2003) that most of the X-ray sources of the XRB are at a redshift lower than 1.5.

As for the individual population contributions, type 1 AGNs are spread over a rather large z-interval to $z > 2$, while type 2 objects and starburst/normal galaxies appear to be more concentrated at $z = 0.5$–1.5. Such evidence of a moderately low median redshift for the sources of the XRB, which we confirm here in a statistical sense, demands significant revision of the XRB synthesis models (Franceschini et al. 2002; Gandhi & Fabian 2003).

We report in Figure 11 the population of the *Chandra*/SWIRE sources in the X-ray luminosity–redshift plane. Here $L_{0.5-8\,\mathrm{keV}}$ is the rest-frame X-ray luminosity $L_X = 4\pi d_L^2 S_X/(1+z)^{1-\alpha_X}$, where d_L is the usual luminosity distance computed for the $H_0 = 71, \Omega_m = 0.27, \Omega_\Lambda = 0.73$ case. The spectral slope (α_X) used to derive the rest-frame luminosities was calculated on the basis of the X-ray hardness ratio (HR) for each source:

$$\alpha_X = \frac{\log[(1-\mathrm{HR})/(1+\mathrm{HR})]}{2\log 2}. \quad (3)$$

The flux S_X is calculated from the observed X-ray count rate adopting the α_X spectral slope, in a consistent way.

After the analysis of Fadda et al. (2002) and Franceschini et al. (2003), the X-ray luminosity is by itself an important discriminant of the primary power sources. On statistical grounds, and also supported by synthetic modeling of the X-ray emission by young stellar populations (Persic et al. 2004), it turns out that an X-ray luminosity of $L_{0.5-8\,\mathrm{keV}} \simeq 3 \times 10^{42}$ ergs s^{-1} ($L_{2-10\,\mathrm{keV}} \simeq 1.5 \times 10^{42}$ ergs s^{-1}) is the maximum achievable by an ultraluminous starburst. This X-ray luminosity corresponds to a rate of star formation of $\sim$1500 $M_\odot$ yr^{-1} assuming a Salpeter stellar initial mass function between 0.1 and 100 $M_\odot$, again a limit achievable by a starburst in the most luminous ULIRGs.

An important conclusion then emerges from the comparison of this limit with the X-ray luminosities estimated for our sources: if we exclude a few among the most local sources, typically at $z < 0.5$, the vast majority exceed this X-ray luminosity value. Our conclusion is that, with few exceptions, our sources are dominated by quasar emission.

A further diagnostic is provided by the ratio of the X-ray to bolometric luminosity L_X/L_{bol}, where L_{bol} is determined from our combined fits of the near-, mid-, and far-IR SEDs. We report in Figure 12 this L_X/L_{bol} luminosity ratio against the total 0.5–8 keV band X-ray luminosity L_X. Our sources display a fairly large range of L_X/L_{bol} values, with the X-ray luminosity ranging from $\sim$0.5% to somewhat more than 10% of L_{bol}. For comparison, in samples of local ULIRGs Braito (2003) and Franceschini et al. (2003) found that a discriminant between a starburst-dominated and quasar-dominated ultraluminous source may be

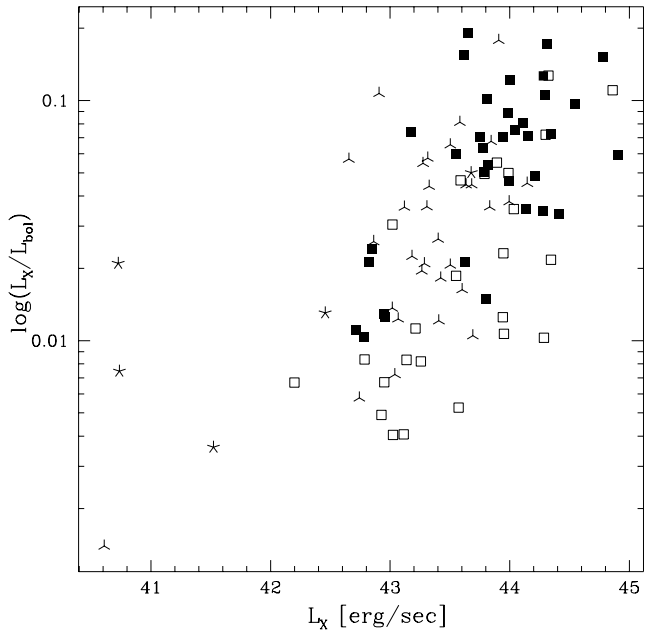

FIG. 12.—Plot of the ratio of the total 0.5–8 keV X-ray to bolometric luminosity as a function of L_X. Symbols are as in Fig. 6.

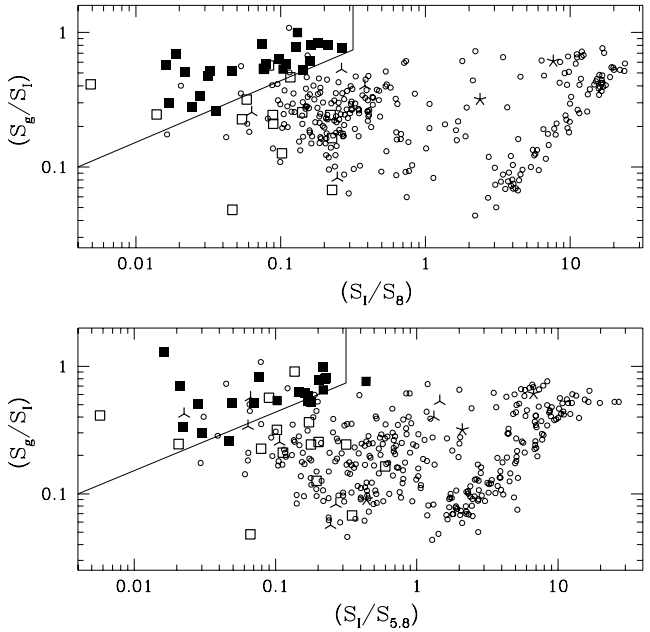

FIG. 13.—Comparison of the optical/IR colors of SWIRE/*Chandra* AGNs (*large symbols*, see legend of Fig. 6) with those of the SWIRE sources without *Chandra* counterparts (*small circles*). The top panel shows the *i*-band to IRAC channel 4 color vs. *g*/*i* color, and the bottom panel uses the *i*-band to IRAC channel 3 color. The region in the upper left corner, delimited by the vertices (−2.4, −1), (−0.5, −0.13), and (−0.5, 1), contains virtually all the *Chandra* type 1 AGNs in both panels. The majority of the type 2 AGNs and of the *Chandra*-undetected galaxies fall outside this region.

set at $L_X/L_{bol} \simeq 2L_{2-10\,keV}/L_{bol} \simeq 10^{-4}$. Indeed, in these studies local ULIRGs with evidence of AGN activity in the IR, like Mrk 231 and the Superantennae, have typical values of the X-ray luminosity around 0.1% of the bolometric luminosity ($L_X/L_{bol} \sim 10^{-3}$). The X-ray prominence of our sample sources is evidently the result of our primary X-ray selection.

On the basis of the results of this section and of Figures 4 and 8, we confirm that, with almost no exception, the combined SWIRE/*Chandra* sources are dominated in X-rays by AGN emission. A dominant fraction of the XRB itself is then proved to come from AGNs.

For more than one-third of these sources (>38%, our classes 3 and 4 plus *Chandra* objects undetected in the IR), our analysis of the optical/IR SEDs did not reveal AGN signatures, although they are AGN-dominated in X-rays. In some cases this lack of evidence may be due to the moderate depth of our survey in the IRAC channels 3 and 4, preventing in half of the sample a proper characterization of the SED at wavelengths (5.8 and 8 μm) at which we would expect the AGN torus emission to emerge. In at least 14 sources, however, the observational SEDs have good IRAC coverage and are indeed best fitted by a starburst/normal galaxy template. In such cases, the only way we can interpret the elusiveness of the AGN in the IR is by assuming a very large dust column density, implying self-absorption in the near-IR torus emission.

3.8. *Statistical Analysis of IR- and X-Ray–Selected SWIRE AGNs*

In an attempt to understand the completeness of our AGN selection, we compare in Figure 13 the optical/IR colors of our SWIRE/*Chandra* AGNs with those of the SWIRE sources without *Chandra* counterparts. In the top panel of the figure we show the *i*-band to IRAC channel 4 color versus the *g*/*i* flux ratio, and in the bottom panel we use the *i*-band to IRAC channel 3 color. The large symbols correspond to our *Chandra* AGNs, whereas the small circles correspond to the SWIRE sources undetected by *Chandra*. It is evident from the figure that a region of the color-color plots (in the upper left corner) identifies in a very efficient way the *Chandra* type 1 AGNs, which are very blue in the optical and very red in the IR. On the other hand, the majority of the type 2 AGNs fall outside this region.

The *Chandra*-undetected sources tend to occupy a complementary region of the color-color plane to that filled by type 1 AGNs. Only a small fraction of *Chandra*-undetected sources (seven in the top and seven in the bottom panels) fall inside it. Then the first important conclusion is that our SWIRE/*Chandra* selection seems rather efficient in identifying the bulk of the type 1 AGN population in the area; if anything, the *Chandra*-undetected sources (making up 90% of the SWIRE population) may hide no more than an additional 20%–30% of the *Chandra* type 1 AGN population.

The second point apparent from Figure 13, however, is that a S_I/S_8 versus S_g/S_I color classification hardly distinguishes the type 2 AGNs: many of the *Chandra* type 2 sources are spread in a region of the plot occupied by X-ray–silent normal and starburst galaxies (we cannot use for the present analysis the optimal $S_H/S_{4.5}$ versus S_H/S_R criterion in Figure 6, because we do not have a full map coverage in the *H* band). In conclusion, we cannot exclude at the present stage that some fraction of the SWIRE population undetected by *Chandra* hides obscured AGNs.

Assuming that we have detected with *Chandra* the bulk of the AGN population in the area, we can derive constraints on the nature of the *Spitzer*-selected sources from a comparison with the X-ray map. We are particularly interested in the sample of MIPS 24 μm sources, since these are expected to contribute substantially to the CIRB. From Papovich et al. (2004) the MIPS source contribution to the CIRB ranges from 40% at $S_{24} > 0.4$ mJy to 80% at $S_{24} > 60$ μJy. The number counts of SWIRE sources in our $17' \times 17'$ *Chandra* field are reported in Figure 1.

We find that above $S_{24} > 0.4$ mJy there are 126 MIPS sources, 18 of which are *Chandra* AGNs (14%). Above 300 μJy there are

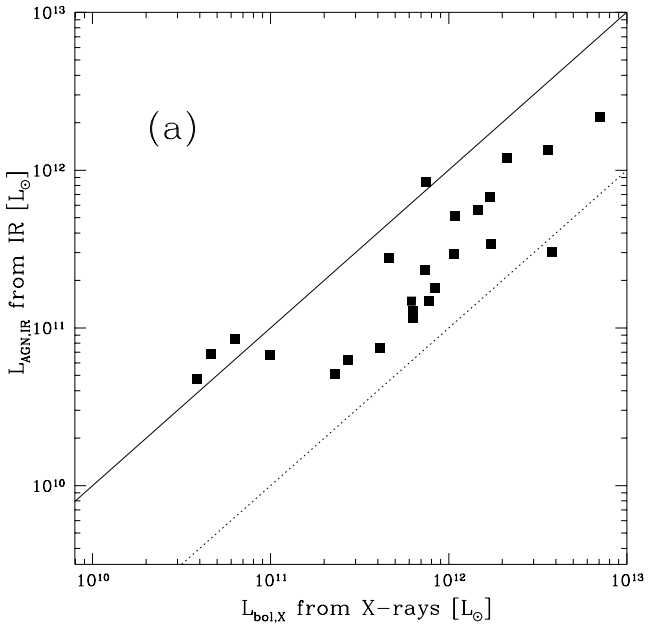

FIG. 14*a*

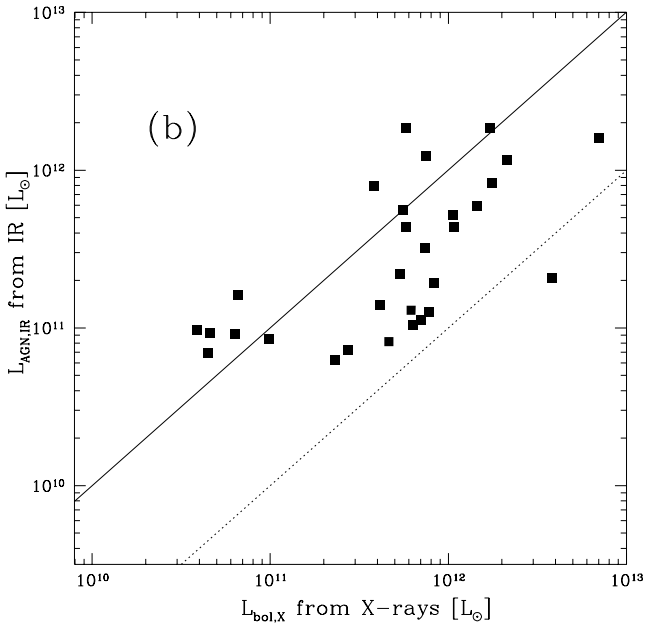

FIG. 14*b*

FIG. 14.—Luminosity of the AGN dust emission component in type 1 AGNs estimated from the *Spitzer* IR luminosity vs. bolometric luminosity derived from the X-ray flux. In (*a*) the dust emission is estimated from the IRAC 8 μm luminosities; in (*b*) it is from the MIPS 24 μm luminosities. The solid line marks a covering fraction of 100% (i.e., $L_{\rm AGN,IR}/L_{\rm bol,X} = 1$), and the dotted line is for a covering fraction of 10%. Only sources detected at 8 and 24 μm are reported in the respective panels.

211 MIPS sources in the *Chandra* field, 27 of which are *Chandra* detections (13%). The fraction of X-ray counterparts decreases steadily at fainter IR fluxes, reaching 9% at 200 μJy (39 *Chandra* out of 433 MIPS sources) and 6% at 100 μJy (59 out of 988). Considering the X-ray to 24 μm flux correlation (Fig. 7), however, this last figure turns out to be already affected by incompleteness due to the X-ray flux limit. These numbers, in any case, have to be increased by a factor of 1.2–1.3 to account for the type 1 *Chandra*-undetected objects (see Fig. 13).

The above numbers appear to be quite consistent with the AGN fraction for faint 15 μm sources estimated by Fadda et al. (2002) at comparable flux limits (>0.4 mJy, for which a 15% $\pm$ 5% AGN fraction was estimated). Our improved statistics and sensitivity below this limit show that the AGN fraction does not seem to increase at fainter fluxes. It remains to be seen, however, whether an additional population of X-ray–weak type 2 AGNs is hidden among SWIRE sources with normal (starburst) optical/IR colors. While an indirect argument against this is mentioned in § 4, quantifying it will require either much deeper X-ray imaging or, better, deep imaging in very hard (>10 keV) X-rays.

3.9. *Estimating the Dust Covering Fraction in AGNs*

To constrain the dust covering fraction in our type 1 AGN sample, we compare in Figure 14 an estimate of the AGN torus luminosity due to dust reradiated emission, directly observed by *Spitzer*, with the AGN bolometric luminosity as inferred from the X-rays. We have estimated the former through the observed source luminosity in the MIPS 24 μm and IRAC 8 μm channels; for type 1 AGNs, these roughly correspond to the expected emission peak by the AGN dust torus for our typical source redshifts (the dust torus emission is expected to peak at $\lambda \sim 5$–10 μm, as observationally seen, e.g., by Elvis et al. [1994], and expected from theoretical modeling; Efstathiou & Rowan-Robinson 1995; Granato et al. 1997). The basic assumption of our analysis is that the fluxes in the 8 and 24 μm channels for our type 1 AGNs are dominated by the AGN torus emission rather than by interstellar medium–reprocessed stellar light, which is supported by the power-law shapes of their IR SEDs shown in Figures 5*a*–5*j*, very inconsistent with those of normal starburst galaxies.

These AGN IR luminosities are compared with the bolometric ones, $L_{\rm bol,X}$, that we estimated from our observed 0.5–8 keV flux of the *Chandra* sources by applying a bolometric correction based on Elvis et al. (1994). To obtain this correction factor, we have integrated their average quasar SED and found a value of $\sim$20 to go from $L_{\rm X}(0.5$–8 keV) to bolometric luminosity.

In the Figure 14*a* the bolometric emission based on the X-ray flux is compared with the AGN IR emission, $L_{\rm AGN,IR}$, estimated from the 8 μm flux as $L_{\rm AGN,IR} = \ln(10)\left[\nu L(\nu)|_{8\mu{\rm m}}\right]$ (corresponding to the energy in one decade in wavelength centered at 8 μm). In Figure 14*b* the comparison is made with the 24 μm–based estimate, $L_{\rm AGN,IR} = \ln(10)\left[\nu L(\nu)|_{24\mu{\rm m}}\right]$.

The bolometric AGN luminosities inferred from the X-ray flux and the AGN IR luminosities turn out to be fairly well correlated in Figure 14*a*, while the correlation is poorer in Figure 14*b* (the 24 μm; see also Fig. 7). The solid and dotted lines in the figure correspond to the predictions in which 100% and 10%, respectively, of the AGN bolometric emission is reprocessed by dust into the IR, assuming that both $L_{\rm AGN,IR}$ and $L_{\rm bol,X}$ are dominated by AGN emission.

Under the same hypothesis of an AGN dominance in the X-ray and 24–8 μm fluxes (argued on the basis of the power-law IR spectra for type 1 AGNs), the position of each source compared with these two lines can be considered to bear an indication of the covering factor of the circumnuclear dust. This covering factor ranges between values of 10% and 100%. Occasionally, $L_{\rm AGN,IR}$ exceeds $L_{\rm bol,X}$, particularly when the former is computed from the 24 μm flux (Fig. 14*b*), which may indicate a possible starburst contribution to the IR emission in some of these sources.

4. DISCUSSION AND CONCLUSIONS

A clear limitation in our analysis can be seen in the shallow depth achieved with the IRAC channels 3 and 4, which would

otherwise be important for source diagnostics. In many instances, even the upper limits of our IRAC survey have set useful constraints on the spectral fits. Deeper IRAC surveys will soon offer such improved capabilities.

We have found that 39% of the *Chandra* sources are dominated by type 1 AGN emission (QSOs or Seyfert 1), 23% are type 2 AGNs, and the remaining 38% are consistent with starburst-like or even normal galaxy spectra in the optical/IR.

On the basis of our estimated X-ray luminosities and the X-ray to IR flux ratios, we have shown that, with few exceptions, all the *Chandra* sources in our sample (including those with galaxy-like optical/IR spectra) are dominated in X-rays by AGN emission. This allows us to estimate the global fraction of type 1 (our class 1) to type 2 AGNs (our classes 2, 3, and 4); assuming conservatively that all *Chandra* sources undetected by SWIRE are type 2 AGNs, the fraction of type 1 AGNs would still be half of the type 2 objects, and the type 1 fraction of the total AGNs would be at least one-third (39 objects out of 119). This type 1 AGN fraction is definitely larger than the canonical value 1/4 to 1/5, or even 1/10, needed to explain the XRB under the strict hypotheses of the standard XRB models (e.g., Comastri et al. 1995; Gilli et al. 2001). A solution is likely to come from Figure 10, showing that an important fraction of the sources of the XRB are found around $z = 1$ (and 70% at $z < 1.5$); the XRB comes mostly from type 2 AGNs at moderate to low z, much lower than previously inferred from type 1 quasar surveys (typically found at $z \sim 2$).

Our analysis of the mid-IR MIPS 24 μm–selected sources, making up much of the CIRB, has shown that the fraction of those sources dominated by an AGN (either type 1 or type 2) is around $\sim$10% to 20% down to 0.3 mJy and may decrease at fainter fluxes. This is consistent with previous findings (Fadda et al. 2002). However, this information does not translate directly into a constraint on the AGN contribution to the CIRB, which is at the moment rather uncertain.

Indeed, the above AGN fraction could be considered as an upper limit to the bolometric AGN contribution to the CIRB, because the AGN IR emission peaks at much shorter wavelengths (rest frame 10 μm) than the CIRB. On the other hand, the available data, like those discussed in the present paper, cannot yet rule out the existence of an additional population of Compton-thick AGNs undetectable in X-rays that could contribute to the CIRB beyond our current 10% limit (e.g., Farrah et al. 2002; Wilman et al. 2003).

It may be worth noting that the locally observed mass density of supermassive black holes (BHs) in galaxies may set a constraint here, although indirect and somehow model dependent. Putting together the optical/X-ray type 1 quasar counts and the XRB spectral intensity, Fabian (2004) (see also Franceschini 2005) argues that, assuming a standard 10% efficiency of gas accretion in AGNs, the whole BH mass density can be explained by normal Compton-thin X-ray/optical AGNs. This sets an upper limit of 20% at most to the local BH density possibly coming from Compton-thick accretion, which implies a modest addition, if any, to the above numbers and a minor contribution altogether by Compton-thick AGNs to the CIRB.

To summarize, we have exploited combined *Chandra* and *Spitzer* multiwavelength imaging and optical/near-IR data to perform a systematic analysis of faint far-IR– and X-ray–selected sources. Our observations substantiate the concept that the two well-separated observational windows tend to select cosmic sources powered by fundamentally different processes, the far-IR probing preferentially stellar thermonuclear reactions, while the X-rays sample AGN accretion. Our results show that the IR observations would be capable of detecting with high efficiency (even at the moderate depths of the SWIRE Legacy survey) the XRB sources. On the other hand, we have shown that for a significant fraction (from 15% up to 40%) of the X-ray/IR sources in common, only deep X-ray observations have revealed the presence of moderately luminous and strongly absorbed AGNs.

Support for this work, part of the *Spitzer Space Telescope* Legacy Science Program, was provided by NASA through an award issued by the Jet Propulsion Laboratory, California Institute of Technology, under NASA contract 1407. This work was also supported by the European Community RTN Network "POE" (grant HPRN-CT-2000-00138).

REFERENCES

Alexander, D. M., Bauer, F. E., Chapman, S. C., Smail, I., Blain, A., Brandt, W. N., & Ivison, J. 2005, in Multiwavelength Mapping of Galaxy Formation and Evolution, ed. R. Bender & A. Renzini (Berlin: Springer), in press (astro-ph/0401129)
Alexander, D. M., et al. 2003, AJ, 125, 383
Almaini, O., Lawrence, A., & Boyle, B. J. 1999, MNRAS, 305, L59
Alonso-Herrero, A., et al. 2004, ApJS, 154, 155
Babbedge, T. S., et al. 2004, MNRAS, 353, 654
———. 2005, in preparation
Barger, A., et al. 2003, AJ, 126, 632
Berta, S., Fritz, J., Franceschini, A., Bressan, A., & Lonsdale, C. 2004, A&A, 418, 913
Berta, S., Fritz, J., Franceschini, A., Bressan, A., & Pernechele, C. 2003, A&A, 403, 119
Bertin, E., & Arnouts, S. 1996, A&AS, 117, 393
Bolzonella, M., Miralles, J.-M., & Pelló, R. 2000, A&A, 363, 476
Braito, V. 2003, Ph.D. thesis, Padova Univ.
Braito, V., et al. 2004, A&A, 420, 79
Brandt, W. N., et al. 2001, ApJ, 558, L5
Brotherton, et al. 2001, ApJ, 546, 775
Cappi, M., et al. 1999, A&A, 350, 777
Comastri, A., Setti, G., Zamorani, G., & Hasinger, G. 1995, A&A, 296, 1
Efstathiou, A., & Rowan-Robinson, M. 1995, MNRAS, 273, 649
Elbaz, D., et al. 2002, A&A, 384, 848
Elvis, M., et al. 1994, ApJS, 95, 1
Fabian, A. C. 2004, in Coevolution of Black Holes and Galaxies, ed. L. C. Ho (Cambridge: Cambridge Univ. Press), 447
Fabian, A. C., & Iwasawa, K. 1999, MNRAS, 303, L34
Fadda, D., et al. 2002, A&A, 383, 838
Farrah, D., et al. 2002, MNRAS, 335, 1163
Franceschini, A. 2005, in Joint Evolution of Black Holes and Galaxies, ed. M. Colpi et al. (Bristol: IOP), in press
Franceschini, A., Aussel, H., Cesarsky, C. J., Elbaz, D., & Fadda, D. 2001, A&A, 378, 1
Franceschini, A., Braito, V., & Fadda, D. 2002, MNRAS, 335, L51
Franceschini, A., et al. 2003, MNRAS, 343, 1181
Freeman, P. E., Kashyap, V., Rosner, R., & Lamb, D. Q. 2002, ApJS, 138, 185
Gandhi, P., & Fabian, A. C. 2003, MNRAS, 339, 1095
George, I. M., Turner, T. J., Netzer, H., Nandra, K., Mushotzky, R. F., & Yaqoob, T. 1998, ApJS, 114, 73
Giacconi, R., et al. 2001, ApJ, 551, 624
Gilli, R., Salvati, M., & Hasinger, G. 2001, A&A, 366, 407
Gilli, R., et al. 2003, ApJ, 592, 721
Gonzalez-Solares, E. A., et al. 2004, MNRAS, submitted (astro-ph/0402406)
———. 2005, in preparation
Granato, G. L., Danese, L., & Franceschini, A. 1997, ApJ, 486, 147
Gregg, M. D., et al. 2002, ApJ, 564, 133
Hasinger, G. 2003, in AIP Conf. Proc. 666, The Emergence of Cosmic Structure: Thirteenth Astrophysics Conference, ed. S. S. Holt & C. S. Reynolds (New York: AIP), 227
Hasinger, G., et al. 2001, A&A, 365, L45
Hauser, M. G., & Dwek, E. 2001, ARA&A, 39, 249
Hauser, M. G., et al. 1998, ApJ, 508, 25
Krabbe, A., Boker, T., & Maiolino, R. 2001, ApJ, 557, 626

Lonsdale, C., et al. 2003, PASP, 115, 897
———. 2004, ApJS, 154, 54
Lutz, D., Maiolino, R., Spoon, H. W. W., & Moorwood, A. F. M. 2004, A&A, 418, 465
Maiolino, R., Ruiz, M., Rieke, G. H., & Keller, L. D. 1995, ApJ, 446, 561
Manners, J. C., et al. 2003, MNRAS, 343, 293
———. 2004, MNRAS, 355, 97
Oliver, S., et al. 2000, MNRAS, 316, 749
Papovich, C., et al. 2004, ApJS, 154, 70
Persic, M., et al. 2004, A&A, 419, 849
Polletta, M. d. C., et al. 2005, in preparation
Prouton, O. R., et al. 2004, A&A, 421, 115
Puget, J.-L., Abergel, A., Bernard, J.-P., Boulanger, F., Burton, W. B., Desert, F.-X., & Hartmann, D. 1996, A&A, 308, L5
Rigby, J. R., et al. 2004, ApJS, 154, 160
Risaliti, G., Gilli, R., Maiolino, R., & Salvati, M. 2000, A&A, 357, 13
Rowan-Robinson, M. 2003, MNRAS, 345, 819
Rowan-Robinson, M., et al. 2005, AJ, 129, 1183
Shupe, D., et al. 2005, in preparation
Silva, L., Granato, G. L., Bressan, A., & Danese, L. 1998, ApJ, 509, 103
Surace, J., et al. 2005, in preparation
Szokoly, G. P., et al. 2004, ApJS, 155, 271
Wilman, R. J., Fabian, A. C., Crawford, C. S., & Cutri, R. M. 2003, MNRAS, 338, L19
Zheng, W., et al. 2004, ApJS, 155, 73